EZH2 Inhibition Induces an Integrated Stress Response Driving Glutamine-Dependent Vulnerability in TNBC

Lucas Porras[1,2], Marina Fukano[3,4], Ann-Sophie Gironne[1,5], Elise Quadri[1,2], Gabriel Alzial[1,2], Hugo Philippeau[1,2], Yousef Aleassa[1,5], Anie Monast[3], Faustine Gorse[1,6], Myriame Saint-Arnaud[1,5], Mariana De Sa Tavares Russo[3], Sylvie Mader[1,2,6], Daina Avizonis[3], Sébastien Lemieux[1,6], Morag Park[3,4], and Geneviève Deblois[1,2,3,5,7*].

[1] Institute for Research in Immunology and Cancer (IRIC), Université de Montréal, Montréal, QC H3C 3J7, Canada.

[2] Department of Molecular Biology, Faculty of Medicine, Université de Montréal, Montréal, QC H3C 3J7, Canada.

[3] Rosalind & Morris Goodman Cancer Institute, McGill University, Montréal, QC H3A 1A3, Canada.

[4] Department of Biochemistry, Faculty of Medicine, McGill University, Montréal, QC H3A 1A3, Canada.

[5] Faculty of Pharmacy, Université de Montréal, Montréal, QC H3C 3J7, Canada.

[6] Department of Biochemistry, Faculty of Medicine, Université de Montréal, Montréal, QC H3C 3J7, Canada.

[7] Lead contact.

* To whom correspondence should be addressed.

Email: genevieve.deblois@umontreal.ca

Keywords: EZH2, dsRNA, integrated stress response, ATF4, amino acid dependency, Glutaminase, Glutaminase inhibitor, triple-negative breast cancer.

ABSTRACT

EZH2, the catalytic subunit of Polycomb Repressive Complex II, is highly expressed and associated with poor prognosis in triple-negative breast cancer (TNBC). Despite inducing significant changes in chromatin profiles and gene expression, EZH2 inhibition in TNBC models has limited impact on growth, suggesting adaptive compensatory mechanisms. Here, we demonstrate that EZH2 inhibition induces accumulation of double-stranded RNA and misfolded proteins in TNBC, activating an integrated stress response (ISR) via the PKR/PERK-eIF2α pathway. We identify Activating Transcription Factor 4 (ATF4) as a key effector upon EZH2 inhibition, driving metabolic changes characterized by increased amino acid uptake and glutamine dependency. Targeting this ISR-ATF4-mediated metabolic response using glutaminase inhibitor in combination with EZH2 inhibition significantly impairs TNBC cell proliferation and tumor progression. These findings reveal a stress-driven metabolic adaptation that enables TNBC survival upon EZH2 blockade, highlighting inhibition of this pathway as a strategy to enhance the efficacy of EZH2 inhibitors in TNBC.

INTRODUCTION

Epigenetic changes are key regulators of tumor progression, enabling transcriptional flexibility for cancer cells to adapt to challenging tumor microenvironments, such as hypoxia, nutrient deprivation, and therapy[1,2]. Dynamic alterations in chromatin structure and accessibility are linked to key tumorigenic processes such as epithelial-to-mesenchymal transition (EMT)[3], immune evasion[4], metastasis[5], and drug resistance[6–8], highlighting epigenetic regulators as promising therapeutic targets to disrupt tumor progression. The Polycomb Repressive Complexes 1 and 2 (PRC1/PRC2) are key components of the Polycomb Group (PcG) proteins that regulate chromatin accessibility by forming facultative heterochromatin domains[9]. In collaboration with PRC1, PRC2 catalyzes the methylation of histone H3 at lysine 27 (H3K27me1/2/3), establishing chromatin states associated with transcriptional repression. PcG complexes are crucial for cell fate determination, repressing developmental genes during embryogenesis and differentiation[10]. Dysregulation of PcG proteins through mutational alterations or aberrant expression is common in cancer[11,12] and can promote tumorigenesis by disrupting PcG-mediated silencing[13].

The catalytic subunits of PRC2, the Enhancer of Zest Homolog 1 and 2 (EZH1/EZH2), drive H3K27me1/2/3 via a SET domain. *EZH2* is frequently overexpressed in solid tumors, including breast, ovarian, endometrial, prostate, liver, lung cancers, and melanoma, where it correlates with tumor progression, metastasis, and drug resistance[14,15]. Somatic mutations in EZH2 are predominantly observed in hematologic malignancies, with gain-of-function mutations driving oncogenic activity in lymphomas[16] and loss-of-function mutations linked to tumor suppressor activity in T-cell leukemias and myelodysplastic syndromes[17,18]. EZH2 activity is also regulated by post-translational modifications, microRNA regulation, and interactions with various protein partners, some of which are independent of PRC2, further underscoring the complexity of EZH2 signaling in tumors. Although EZH2 is an attractive anticancer target, preclinical studies show variable inhibitor activity and frequent resistance. More pronounced effects are seen in hematologic malignancies, particularly germinal-center lymphomas with EZH2 mutations, as well as adult T-cell leukemia/lymphoma and multiple myeloma[19–21]. Clinically, the EZH2 inhibitor tazemetostat (TAZVERIK) has received accelerated approval for the treatment of epithelioid sarcoma and for relapsed/refractory follicular lymphoma with EZH2 mutations[22], demonstrating modest activity with durable responses in a subset and a generally manageable safety profile[23]. By

contrast, preclinical solid-tumor models often show limited benefit from EZH2 inhibition, with clearer responses in specific genetic contexts (e.g., ARID1A-deficient ovarian cancer) [24,25]. This limited efficacy likely reflects adaptive tumor biology, including rewiring of DNA-damage responses, metabolism, and immune signaling[26–32], supporting rational combination strategies as the path forward.

In breast cancer, EZH2 is overexpressed in the basal-like subtype, enriched for Triple-Negative Breast Cancer (TNBC), a highly aggressive subtype negative for estrogen and progesterone receptors, as well as HER2 amplification. TNBCs are associated with poor outcomes and high relapse rates following chemotherapy[33]. Elevated *EZH2* expression in basal-like breast tumors is associated with advanced stages, chemoresistance, metastasis, and poor prognosis[34–36]. Although EZH2 is linked to aggressive TNBC phenotypes, its targeting in preclinical models often yields inconsistent and modest effects on tumor growth, despite the complete loss of the H3K27me3 mark, which is in line with observations in other solid malignancies[7,8,34]. The limited efficacy suggests activation of compensatory mechanisms that sustain tumor growth, resulting in tolerance to EZH2 inhibition. These observations underscore the need for further mechanistic studies to better understand the molecular consequences of inhibiting EZH2 in TNBC and to optimize its potential for rational combination-based therapeutic strategies[37].

Here, we investigate the molecular consequences of targeting EZH2 in TNBC to uncover vulnerabilities that could be exploited for therapeutic treatment. Our data reveal that pharmacological inhibition or depletion of EZH2 leads to the accumulation of double-stranded RNA (dsRNA) and misfolded proteins in TNBC cells and patient-derived xenografts (PDX). These further converge in activating an integrated stress response (ISR) via the activation of the Protein Kinase R (PKR) and Protein Kinase RNA-like Endoplasmic Reticulum Kinase (PERK) - eukaryotic Initiation Factor 2 Alpha (eIF2α) (PKR/PERK-eIF2α) signaling axis. We identified that elevated levels of Activating Transcription Factor 4 (ATF4), a key effector of the ISR pathway, in response to EZH2 inhibition drive an adaptive metabolic response enhancing amino acid uptake and glutamine metabolism, supporting cell survival and limiting tumor regression. Disrupting this ISR-ATF4-mediated metabolic response with a Glutaminase (GLS) inhibitor enhanced the efficacy of EZH2 inhibition, offering a strategy to sensitize TNBC to EZH2 targeting.

RESULTS

EZH2 Inhibition Promotes an Epigenetic Switch Driving dsRNA Accumulation in TNBC.

Given the association between EZH2 overexpression and poor prognosis in TNBC[33], we explored the molecular consequences of inhibiting EZH2 in TNBC. We confirmed that treatment of TNBC PDXs (GCRC1915 and GCRC1939) with the EZH1/2-targeting chemical probe UNC1999 *in vivo* (300 mg/kg, 21 days) results in a significant reduction of H3K27me3 levels, as shown by immunohistochemistry (IHC) (Fig. **1A** and **S1A**) and immunoblotting (Fig. **1B** and **S1B**), without inducing the apoptotic marker Cleaved Caspase-3 (Fig. **S1C** and **S1D**) or affecting PDX progression (Fig. **1C**), as previously observed[7]. Consistent with previous findings[38], the global levels of H3K27ac, associated with accessible chromatin, are increased following EZH2 inhibition and H3K27me3 loss in TNBC PDX. Similar observations are obtained in TNBC cell lines MDA-MB-436 and Hs 578T exposed to UNC1999 (1 μM, 96 h) or EZH2-selective small-molecule inhibitor EPZ-6438 (1 μM, 96 h) (Fig. **1D** and **S1E-F**). CRISPR/Cas9 sgRNA-mediated deletion of *EZH2* in MDA-MB-436 cells also resulted in a significant loss of global H3K27me3, accompanied by a concomitant increase in H3K27ac levels (Fig. **1E** and **S1G**), without affecting cell growth compared to wild-type cells (Fig. **S1H**). These observations indicate that, despite a marked loss of H3K27me3 and an increase in H3K27ac levels following EZH2 inhibition or deletion, TNBC growth remains largely unaffected, suggesting the activation of compensatory mechanisms that sustain TNBC cell proliferation and tumor progression.

To investigate epigenetic reprogramming induced by EZH2 inhibition in TNBC, we performed chromatin immunoprecipitation sequencing (ChIP-seq with exogenous *Drosophila* spike-in normalization) for H3K27 modification marks. A marked decrease in the intensity and number of H3K27me3 loci is observed in GCRC1915 PDX exposed to UNC1999 *in vivo* (300 mg/kg, 21 days) compared to vehicle controls (Fig. **1F**). EZH2 inhibition also resulted in a significant increase in global H3K27ac signal intensity and in peak number (6127 H3K27ac peaks gained) (Fig. **1G** and **S1I**). Genomic loci that lose H3K27me3 following UNC1999 treatment in TNBC PDX (13,325) were globally associated with a gain of H3K27ac (Fig. **1H**; r = -0.3905). Conversely, the 6,127 loci that gain H3K27ac upon EZH2 inhibition are also associated with H3K27me3 loss, albeit with more variation (Fig. **S1J**; r = -0.2735, most loci are in the upper left quadrant). As expected, the distribution of H3K27me3 peaks is predominantly intergenic and

intronic (62.1%, Fig. **1I**, bottom). Notably, H3K27ac loci detected following exposure to UNC1999 exhibit a higher enrichment in distal intergenic and intronic regions (51.4%) compared to untreated tumors (44.6%) (Fig. **1I**, middle vs. top panels), suggesting increased accessibility at non-coding genomic regions following EZH2 inhibition. An enriched intergenic H3K27ac signal, coinciding with H3K27me3 loss, is also observed in MDA-MB-436 cells exposed to UNC1999 (1 μM, 96 h) (Fig. **S1K-M**). Together, these results reveal an epigenetic rewiring from H3K27me3 to H3K27ac, indicative of increased chromatin accessibility at non-coding DNA in response to EZH2 inhibition in TNBC.

To assess the functional impact of this epigenetic shift, we analyzed transcriptional changes following EZH2 inhibition in TNBC PDX models and cell lines. Gene set enrichment analysis (GSEA) revealed significant enrichment of interferon (IFN) alpha and gamma response pathways, as well as KRAS signaling, cell cycle and E2F pathways, among the upregulated genes in UNC1999-treated TNBC PDX compared to controls (Fig. **1J-K**). A similar enrichment in IFN response pathways was observed in MDA-MB-436 and Hs 578T cells exposed to UNC1999 or EPZ-6438 (Fig. **S1N**). The IFN response can be triggered by cellular accumulation of double-stranded RNA (dsRNA) in response to transposable element (TE) expression. Loci showing H3K27me3 loss and H3K27ac gain following EZH2 inhibition in TNBC PDX are enriched for TE families that are localized within these peaks and that can form dsRNA (LTR (ERV1, ERVL/K), Retroposons (LINE-1 (L1), SINE (eg. Alu)) (Fig. **S1O-R**), which are usually silenced by heterochromatin. Transcriptional upregulation of the LTR, L1, and SVA families is observed following EZH2 inhibition in tumors (Fig. **1L-M**). Immunofluorescence (IF; J2 antibody) revealed increased dsRNA and decreased H3K27me3 levels in TNBC PDXs GCRC1915 and GCRC1939 exposed to UNC1999 (Fig. **1N-O** and **S1S**). Similar results were obtained in MDA-MB-436 cells exposed to UNC1999 or EPZ-6438, as demonstrated by immunofluorescence (Fig. **1P-Q**), and further confirmed by flow cytometry quantification (Fig. **1R**). Together, these findings indicate that EZH2 inhibition induces an epigenetic change from repressive to accessible chromatin in TNBC at loci enriched for TE, leading to TE expression, dsRNA accumulation, and activation of IFN response genes.

Induction of Integrated Stress Response Enables TNBC Cell Survival upon EZH2 Inhibition.

During cellular stress, sensing of dsRNA by Protein Kinase R (PKR) activates dimerization and autophosphorylation at threonine 446 (pT446), leading to phosphorylation of eIF2α at serine 51 (pS51) (Fig. **2A**). This suppresses global translation while selectively promoting stress-adaptive mRNA translation, such as that of the Activating Transcription Factor 4 (ATF4). Such a cascade of events triggers an Integrated Stress Response (ISR) known to modulate cell fate under stress.

We confirmed the significant induction of pT446-PKR following EZH2 inhibition in TNBC PDX models (GCRC1915, GCRC1939; UNC1999, 300 mg/kg) (Fig. **2B** and **S2A-C**) and MDA-MB-436 cells (Fig. **2C** and **S2D**) using immunoblotting. We further observed pS51-eIF2α and ATF4 induction in TNBC PDXs GCRC1915 and GCRC1939 (UNC1999, 300 mg/kg; 21 days) using immunoblotting and IHC (Fig. **2D-E**, **S2B-C** and **S2E-F**) and cell lines MDA-MB-436 and Hs 578T (UNC1999/EPZ-6438, 1 μM, 48 h) (Fig. **2F** and **S2G-I**). ATF4 is also significantly induced in EZH2-KO MDA-MB-436 cells compared to sgControl cells (Fig. **2G** and **S2J**). We then examined the induction of other ISR-related kinases and observed phosphorylation (pT980) of PKR-like endoplasmic reticulum kinase **(**PERK) in response to EZH2 inhibition in PDX models and cell lines, but not of the General Control Nonderepressible-2 kinase (GCN2) (pT899) (Fig. **2H-I** and **S2K-N**). PERK is typically activated by an overload of misfolded proteins. We confirmed accumulation of misfolded proteins following UNC1999 or EPZ-6438 exposure in TNBC cells using the TPE-MI thiol probe, which detects free cysteine thiols within proteins. (Fig. **2J-K**, **S2O-P**).

To evaluate the importance of ISR induction in response to EZH2 inhibition, we depleted core ISR components using siRNAs in MDA-MB-436 and Hs 578T cells (Fig. **2L** and **S2Q**). Depletion of *PERK*, *PKR*, or *EIF2A*, but not *GCN2*, significantly impaired MDA-MB-436 cell viability only when exposed to UNC1999 (1 μM, 96 h) (Fig. **2M** and **S2R**). Likewise, siRNA-mediated *ATF4* depletion in MDA-MB-436, Hs 578T, and GCRC1915-PDC (derived from CGCR1915 PDX) modestly reduced viability (10–25%) under basal conditions but led to significant decrease in viability (80–95%) along with a significant induction of the apoptotic marker cleaved poly (ADP-ribose) polymerase (cl-PARP) upon UNC1999 treatment (Fig. **2N-O** and **S2S-U**). Together, these findings reveal that EZH2 inhibition induces an ISR via the PKR/PERK/eIF2α/ATF4 axis in response to the accumulation of dsRNA and misfolded proteins in TNBC. Importantly, induction of this stress response appears essential to sustain TNBC cell viability upon EZH2 inhibition.

ATF4 Regulates an Amino Acid Gene Signature in Response to EZH2 Inhibition in TNBC.

Given the role of ATF4 in stress adaptation, we examined its function as an ISR effector in response to EZH2 inhibition in TNBC. GSEA of differentially expressed genes in GCRC1915 PDX and MDA-MB-436 cells exposed to UNC1999 or control revealed the enrichment of previously identified ATF4 target genes[39] (Fig. **3A**). EZH2 inhibition using UNC1999 in GCRC1915 PDX and UNC1999 or EPZ-6438 in TNBC cell lines significantly increased the expression of ATF4 target genes involved in amino acid transport (e.g., *SLC7A5, SLC7A11, SLC3A1, SLC1A4, SLC1A5,* etc.), antioxidant response (e.g., *SLC7A11, SLC3A2*), and amino acid metabolism (e.g., *PSAT1, BCAT1*, *ASNS* etc.) (Fig. **S3A-B**). Protein level validation using IHC and immunoblotting confirmed significant increase in amino acid transporters LAT1 (*SLC7A5*), CD98 (*SLC3A2*), ASCT2 (*SLC1A5*), xCT (*SLC7A11*), and metabolic enzymes PSAT1, BCAT1, and ASNS, following EZH2 inhibition in GCRC1915 PDX (UNC1999) and TNBC cell lines (UNC1999 and EPZ-6438) (Fig. **3B-D** and **S3C-D**).

Using siRNAs, we next show that ATF4 depletion in MDA-MB-436 cells significantly abrogates the UNC1999-dependent increase in amino acid transporters and metabolic enzymes at the protein level (Fig. **3E** and **S3E-G**). GSEA analyses of transcriptomic data from ATF4-depleted MDA-MB-436 relative to siControl cells (RNA-seq, Fig. **3F**) shows that downregulated genes following ATF4 depletion upon EZH2 inhibition are significantly enriched for ISR-related pathways (tRNA aminoacylation, PERK, HRI, ATF4, GCN2) and amino acid transport/metabolism (Reactome, FDR $q < 0.05$) (Fig. **3G**). Notably, genes upregulated upon exposing TNBC cells to UNC1999 show a trend of reduced expression upon ATF4 depletion in MDA-MB-436 cells (Fig. **3H**; $r = -0.451$, p-value<0.0001), including genes encoding amino acid transporters and metabolic enzymes (Fig. **3I**). Interestingly, ATF4 depletion also upregulates genes associated to mRNA translation, senescence, apoptosis, and ferroptosis (Fig. **S3H**), highlighting the protective role of ATF4 against cell death upon EZH2 inhibition. Finally, we employed chromatin immunoprecipitation (ChIP) followed by quantitative PCR (qPCR) in GCRC1915 PDX and MDA-MB-436 cells to demonstrate that EZH2 inhibition using UNC1999 induces ATF4 enrichment at the promoters of selected amino acid transport and metabolism genes (*ASNS, BCAT1, PSAT1, SLC7A11*) (Fig. **3J** and **S3I**). Together, these findings demonstrate that ATF4 induction in response to EZH2 inhibition in TNBC plays a critical role in regulating the expression of key genes involved in amino acid homeostasis, antioxidant response, and cell survival.

EZH2 Inhibition Induces ATF4-Mediated Metabolic Adaptation in TNBC.

Given the ATF4-driven induction of amino acid transporters and metabolic enzymes following EZH2 inhibition, we assessed the metabolic impact of inhibiting EZH2 by analyzing amino acid uptake and release in TNBC cells. Metabolite quantification from conditioned media of MDA-MB-436 and Hs 578T cells by Nova Bioprofiler revealed significantly increased glutamine uptake and elevated glutamate release following treatment with UNC1999 or EPZ-6438 (72 h) compared to mock-treated cells (Fig. **4A**). Glucose uptake and lactate release remained unaffected (Fig. **S4A**). Further amino acid quantification in conditioned media using Triple quadrupole-liquid chromatography-mass spectrometry (LC-QQQ-MS; Intrada-amino-acids) revealed significant changes in amino acid uptake and release following EZH2 inhibition (1 μM UNC1999 or EPZ-6438; 72 h) in MDA-MB-436 and Hs 578T cells compared to control (Fig. **4B** and **S4B**). Specifically, EZH2 inhibition significantly enhanced the uptake of branched-chain amino acids (BCAAs: leucine, valine, isoleucine), serine, glutamine, methionine, and cystine, while promoting glutamate release. The xCT/CD98 antiporter mediates cystine import and glutamate export, supporting glutathione-dependent antioxidant defense. Uptake of glutamine, BCAAs (via transamination), and methionine further sustains this response by replenishing intracellular glutamate and contributing to glutathione biosynthesis (Fig. **4C**). We show that ATF4 depletion in MDA-MB-436 cells significantly reduces the uptake of these amino acids following UNC1999 or EPZ-6438 treatment (60h), highlighting the key role of ATF4 in this metabolic adaptation to EZH2 inhibitors (Fig. **4D**). Quadrupole time of flight-liquid chromatography-mass spectrometry (LC-QTOF-MS, Ion-pairing) analysis of intracellular metabolites from Hs 578T cells exposed to UNC1999 (1 μM, 72 h) revealed a significant increase in intracellular glutamate, α-ketoglutarate (αKG), oxidized glutathione, asparagine, fumarate and malate levels (Fig. **4E** and **S4C**). Accordingly, stable isotope labeling with $^{13}C_5$-glutamine revealed significantly increased glutamine-derived carbon incorporation into glutamate and αKG, indicating enhanced glutaminolysis following EZH2 inhibition by UNC1999 in Hs 578T cells (Fig. **4F**). Additionally, we observed that glutamine-derived carbon incorporation is modestly but significantly decreased into metabolites of the oxidative branch of the TCA cycle (m+4) while showing a modest increase in metabolites produced via reductive carboxylation (m+3) (Fig. **S4D-E**). No change was observed in ^{13}C incorporation into gamma-aminobutyric acid (GABA), a glutamate-derived metabolite that serves as an alternative route into the TCA cycle (Fig. **S4F**). Seahorse XFe96 analysis revealed no

significant changes in oxygen consumption rates (OCR) or extracellular acidification rates (ECAR) under basal or stressed conditions in MDA-MB-436 and Hs 578T cells following EZH2 inhibition (UNC1999 or EPZ-6438) (Fig. **S4G-H**). Together, these results indicate that EZH2 inhibition promotes an ATF4-driven metabolic adaptation in TNBC cells, enhancing amino acid uptake and glutamate release, which could support glutaminolysis, transamination, and antioxidant defense.

Glutaminase Inhibition Prevents Metabolic Adaptations and Sensitizes TNBC to EZH2 Inhibition.

To assess whether ISR-ATF4-dependent amino acid metabolism rewiring is crucial for TNBC cell survival and proliferation in response to EZH2 inhibition, we exposed TNBC cells to glutamine deprivation or regular media (0.08 vs 4 mM glutamine) for 96 h. Treatment with UNC1999 (1 μM) selectively reduced cell viability under low-glutamine conditions, indicating increased glutamine dependency in TNBC cells following EZH2 inhibition (Fig. **5A**). Consistently, the levels of glutaminase (GLS), which catalyzes glutamine hydrolysis into glutamate and ammonia as the first step of glutaminolysis, are significantly upregulated upon EZH2 inhibition with UNC1999 or EPZ-6438 in TNBC cells (Fig. **5B** and **S5A**), as well as in TNBC PDX models GCRC1915 and GCRC1939 treated with UNC1999 (300 mg/kg, 21 days), as shown by IHC and immunoblotting (Fig. **5C-D**, **S5B-E**). Notably, siRNA-mediated ATF4 depletion significantly blunted the UNC1999-induced GLS increase in TNBC cells (Fig. **5E** and **S5F**), indicating that EZH2 inhibition promotes GLS upregulation via ATF4 signaling in TNBC.

To investigate whether GLS induction supports TNBC survival and proliferation upon EZH2 inhibition, we exposed TNBC cells to the selective GLS inhibitor Telaglenastat (CB-839; trial #NCT03057600). Dose-response analysis showed that CB-839 significantly sensitizes MDA-MB-436, Hs 578T, and GCRC1915-PDC cells to EZH2 inhibition by UNC1999 or EPZ-6438 (1 μM) (Fig. **5F** and **S5G**). GLS levels are also significantly elevated in EZH2-deleted (sg*EZH2*) MDA-MB-436 cells compared to cells with the sgControl (Fig. **5G** and **S5H**). Notably, CB-839 selectively impaired the growth of EZH2-deleted MDA-MB-436 cells with minimal impact on sgControl cells (Fig. **5H**), indicating that EZH2 loss also sensitizes TNBC cells to GLS inhibition. We further validated that depletion of GLS using specific siRNAs also sensitized TNBC cells to EZH2 inhibition (Fig. **S5I**).

To assess the effects of combining EZH2 and GLS inhibition *in vivo*, we implanted GCRC1915 PDX in NOD scid gamma (NSG) mice and exposed mice to UNC1999 (150 mg/kg, 5x/week), CB-839 (200 mg/kg, daily), or both. Combined EZH2-GLS inhibition significantly reduced tumor volume compared to control or single-agent treatments (Fig. **5J-K**) without affecting body weight (Fig. **S5J**). Immunoblotting of end-point tumors confirmed the induction of ATF4 and GLS levels in UNC1999-treated PDXs (Fig. **5I**). Importantly, the UNC1999/CB-839 combination significantly increased cl-PARP and cl-Caspase3 whereas individual treatments did not, indicating effective cell death induction specifically upon combined EZH2/GLS inhibition in TNBC PDX (Fig. **S5K**). Combined EZH2/GLS inhibition did not increase ATF4, GLS, or cl-PARP levels in normal tissues, as shown in liver (Fig. **S5L**), suggesting a tumor-specific effect. Similarly, CB-839 treatment (200 mg/kg) of NSG mice bearing EZH2-deleted Hs 578T cells (sgEZH2) xenografts significantly reduced tumor growth compared to sgControl xenografts (Fig. **S5M**). CB-839 treatment also resulted in increased ATF4, GLS, and induced cl-PARP levels in this model, without affecting total body weight compared to sgControls (Figure **S5N-P**). Together, these findings demonstrate that targeting glutamine-dependent metabolic rewiring, induced in response to EZH2 inhibition via an ISR-ATF4 axis, sensitizes TNBC cells and tumors to EZH2 inhibition or deletion.

DISCUSSION

This study investigates the intricate response of TNBC to EZH2 inhibition, revealing a coordinated interplay between epigenetic dysregulation, cellular stress induction, and adaptive metabolic reprogramming. Although EZH2 inhibition triggers widespread epigenetic changes and elicits multiple cellular stresses potentially detrimental to cancer cells, including dsRNA accumulation and misfolded proteins, it does not systematically impair TNBC cell proliferation, viability, or tumor growth. We demonstrate that TNBC cells maintain survival and proliferative capacity upon EZH2 inhibition by activating an ISR, which drives adaptive metabolic reprogramming. ATF4 emerged as a key mediator of this ISR, orchestrating a metabolic program essential for cell survival and sustained proliferation under EZH2-inhibited conditions. Notably, we demonstrate that disrupting this adaptive response, specifically by targeting glutamine metabolism through GLS inhibition, sensitizes TNBC cells and tumors to EZH2 inhibitors, highlighting a potential targeting strategy for TNBC.

EZH2 is emerging as a promising therapeutic target in cancer due to its central role in regulating gene expression and cell identity via histone modification. EZH2 has been implicated in multiple cancer-related processes, including cell proliferation, invasion, and senescence, underscoring its significance in tumor progression[27,40,41]. The development of pharmacological EZH2 inhibitors has garnered considerable attention, as evidenced by the FDA approval of Tazemetostat for epithelioid sarcoma and follicular lymphoma[22]. However, recent studies have revealed the complexity of targeting EZH2, as its inhibition does not uniformly suppress tumor growth and, in specific contexts, may even promote tumorigenesis[42]. The tumor microenvironment also modulates EZH2 activity. For instance, hypoxia and inflammation can regulate EZH2 expression through HIF1α[43] and NF-κB/STAT3 signaling[44], while nutrient availability can impact its activity via metabolic signaling[45]. Further complicating its targeting outcomes, EZH2 also exhibits PRC2-independent functions, which have been observed in TNBC[46] and may persist despite EZH2 inhibition, contributing to tumorigenesis through alternative mechanisms. Whether PRC2-independent/non-canonical activities of EZH2 play a role in the ISR-ATF4-driven metabolic reprogramming described in this study remains to be determined. These complexities underscore the need for a comprehensive understanding of the multifaceted roles of EZH2 across cancer contexts to optimize targeting strategies and minimize adverse effects.

We demonstrate that EZH2 inhibition triggers an epigenetic switch characterized by a reciprocal gain in H3K27ac upon H3K27me3. Previous studies reported that this switch may serve as a transcriptional driver of resistance to EZH2/PRC2 inhibition by activating oncogenic pathways[37,47]. In TNBC, H3K27ac levels increase not only at promoters of oncogenic genes (e.g., KRAS, EMT-related genes) but also at intergenic regions, suggesting that H3K27me3 loss enhances chromatin accessibility at distal regulatory elements. This chromatin remodeling coincides with the enrichment and increased expression of TEs, including endogenous retroviruses (ERVs) and LINE-1, in both TNBC cells and PDX models. These findings implicate EZH2 in the repression of dsRNA-forming elements, supporting the notion that its inhibition promotes dsRNA accumulation. Promoters gaining H3K27ac upon EZH2 inhibition are also enriched in interferon (IFN) response, viral mimicry, and IL2/STAT5 signaling pathways, linking H3K27ac reprogramming to dsRNA sensing and IFN activation. Notably, these promoters were not marked by H3K27me3 before EZH2 inhibition, indicating that IFN gene activation occurs through indirect epigenetic remodeling rather than direct PRC2 control. Targeting this compensatory epigenetic adaptation may enhance the efficacy of EZH2 inhibitors[48]. Indeed, inhibition of bromodomains, p300, or MLL has been shown to improve EZH2 inhibitor responses by suppressing oncogene expression[37], and HDAC inhibitors synergize with EZH2 inhibitors by inducing the expression of pro-apoptotic genes[49]. Likewise, combining EZH2 inhibition with PRMT1 or DNMT inhibitors has shown synergistic effects[50,51], underscoring the therapeutic potential of co-targeting compensatory epigenetic mechanisms to improve responses to EZH2 inhibition. Future studies should explore whether such combinations modulate TE expression and dsRNA induction.

EZH2 inhibition with GSK343 and UNC1999 has previously been shown to induce autophagy-related genes and ER stress/UPR-associated transcripts, promoting colon cancer cell survival[52]. While we did not observe significant transcriptional regulation of these pathways in TNBC upon EZH2 inhibition, we found that EZH2 inhibition led to the accumulation of misfolded proteins and PERK activation, contributing to ISR in our model. Increased chromatin accessibility may enable the transcription of cryptic proteins that contribute to the accumulation of misfolded proteins and ER stress. Alternatively, ER stress may result from dsRNA accumulation, as PKR-mediated eIF2α phosphorylation impairs ribosomal function, leading to the accumulation of misfolded proteins and PERK activation[53]. However, PERK activation occurred independently of dsRNA-PKR activation in Hs 578T cells, suggesting that EZH2 inhibition can induce UPR independently.

Further studies are needed to elucidate the mechanisms linking EZH2 inhibition to UPR induction in TNBC, and to determine whether prolonged activation of this stress response could become detrimental to TNBC cell survival.

The dsRNA accumulation and downstream IFN response arise from increased intergenic chromatin accessibility and TE derepression. While TEs are primarily silenced by DNA and H3K9 methylation, PRC2 can also contribute to their repression, particularly when other silencing marks are diminished[7,54]. We previously demonstrated that paclitaxel-resistant TNBC cells compensate for intergenic DNA hypomethylation by redistributing H3K27me3 to maintain TE repression[7]. Due to low DNA methylation levels, these paclitaxel-resistant cells became highly dependent on H3K27me3 repression of TEs and sensitive to EZH2 inhibition, which resulted in excessive dsRNA accumulation and cell death. Here we show that in absence of paclitaxel,TNBC PDXs display dsRNA induction in response to EZH2 inhibition, albeit at lower levels and without impairing tumor growth, due to ISR-dependent metabolic adaptation that supports cell survival. These findings suggest that the relative levels of DNA and H3K9 methylation in a tumor may dictate sensitivity to EZH2 inhibitors. Supporting this, co-inhibition of DNMT and EZH2 has been shown to synergistically amplify dsRNA-IFN signaling and promote cancer cell death in multiple tumor models[55]. It is also possible that the TEs induced following the loss of H3K27me3 lead to quantitative or qualitative differences in viral mimicry responses compared to those induced upon blocking DNA methylation or H3K9me2/3[54]. Furthermore, our observation that EZH2 inhibition activates a cell-autonomous innate immune response suggests potential immunotherapy applications in TNBC. Accordingly, EZH2 inhibition has been shown to trigger a dsRNA-STING-IFN signature in various cancer cells and to upregulate antigen presentation genes, including PD-L1[56,57]. Exposing these models to EZH2 inhibitors enhanced $CD8^+$ T cell infiltration and M1 macrophage polarization, ultimately improving response to PD-1 checkpoint inhibitors. Whether similar immunomodulatory effects occur in TNBC in response to EZH2 inhibition remains to be further explored.

ATF4 is a central transcription factor that orchestrates cellular responses to stressors such as nutrient deprivation, viral infection and ER stress, primarily by activating ISR in tumors[58]. ATF4 drives functions that support tumor survival, progression, and resistance to therapy by regulating the expression of genes involved in amino acid metabolism, glucose utilization, autophagy, redox homeostasis, and stress adaptation[59]. Previous studies have reported increased ATF4 levels in

prostate cancer cell lines following EZH2 inhibition[56]. Our findings highlight ATF4 as a key integrator of the ISR and metabolic adaptation in response to EZH2 inhibition, resulting in altered expression of metabolic genes and changes in amino acid uptake. Further studies are needed to assess whether additional stress-responsive transcription factors such as STAT1 or NRF2 also contribute to metabolic rewiring following EZH2 inhibition in TNBC. Alternatively, ATF4 can also induce apoptosis under severe or sustained stress[60]. Its role in determining cell fate is context-specific, depending on the nature and magnitude of the stress. The mechanisms by which ATF4 regulates survival versus death in the context of EZH2 inhibition remain to be delineated in TNBC, as it is conceivable that sustained ISR induction upon EZH2 inhibition may become detrimental to TNBC cells.

Inhibition of EZH2 has been associated with metabolic rewiring in various cancer models[29,30]. In TNBC we show that it induces a stress-driven glutamine dependence that can be co-targeted with EZH2. Given the limited specificity and clinical progress of available ISR–ATF4 inhibitors, we prioritized the inhibition of GLS. Telaglenastat (CB-839) is a clinically advanced GLS1 inhibitor, including in TNBC, where it showed clinical activity but heterogeneous responses[61], indicating the need for better predictive markers (#NCT02071862; NCT03057600). Co-targeting EZH2 and GLS offers a rational path to increase efficacy, potentially lower EZH2-inhibitor dose requirements, and broaden the benefit of CB-839 in triple-negative breast cancer. Future studies should evaluate additional EZH2–GLS combinations (eg. IACS-6274, BPTES) to refine efficacy, explore alternative adaptations and delineate toxicity.

Together, this work enhances our understanding of the molecular mechanisms governing TNBC's response to EZH2 inhibition, elucidating the adaptive mechanisms that allow TNBC cells to survive the loss of EZH2 activity. Importantly, our work provides valuable insights into the development of effective therapeutic strategies targeting epigenetic and metabolic pathways in TNBC.

KEY RESSOURCES TABLE

REAGENT or RESOURCE	SOURCE	IDENTIFIER
Antibodies		
EZH2	Cell Signaling Technology	Cat#5246; RRID: AB_10694683
H3K27me3	Cell Signaling Technology	Cat#9733; RRID: AB_2616029
H3K27Ac	Abcam	Cat#ab4729; RRID: AB_2118291
H3	Abcam	Cat#ab10799; RRID: AB_470239
dsRNA	EMD Millipore	Cat#MABE-1134; RRID: AB_2819101
pT446-PKR	Abcam	Cat#ab32036; RRID: AB_777310
PKR	Cell Signaling Technology	Cat#12297; RRID: AB_2665515
pT980-PERK	Cell Signaling Technology	Cat#3179; RRID: AB_2095853
PERK	Cell Signaling Technology	Cat#3192; RRID: AB_2095847
β-actin	Sigma-Aldrich	Cat#A5441; RRID: AB_476744
pT899-GCN2	Abcam	Cat#ab75836; RRID: AB_1310260
GCN2	Cell Signaling Technology	Cat#3302; RRID: AB_2277617
pS51-eIF2α	Cell Signaling Technology	Cat#9721; RRID: AB_330951
eIF2α	Cell Signaling Technology	Cat#9722; RRID: AB_2230924
ATF4 (IHC)	Abcam	Cat#ab31390; RRID: AB_725568
ATF4 (immunoblot and ChIP)	Cell Signaling Technology	Cat#11815; RRID: AB_2616025
α-tubulin	Sigma-Aldrich	Cat#T5168; RRID: AB_477579
Cleaved-PARP	Cell Signaling Technology	Cat#9541; RRID: AB_331426
PARP	Cell Signaling Technology	Cat#9542; RRID: AB_2160739
Lamin B1	Abcam	Cat#ab16048; RRID: AB_443298
LAT1	Cell Signaling Technology	Cat#32683; RRID: AB_3265513
CD98	Cell Signaling Technology	Cat#47213; RRID: AB_2799323
ASNS	Cell Signaling Technology	Cat#92479; RRID: AB_3082991
BCAT1 (for immunoblot)	Cell Signaling Technology	Cat#12822; RRID: AB_2798035
BCAT1 (for IHC)	Origene	Cat#TA504360; RRID: AB_11126287
PSAT1	NOVUS Biological	Cat#NBP1-32920; RRID: AB_2172600
GLS	Abcam	Cat#ab156876; RRID: AB_2721038
xCT	Cell Signaling Technology	Cat#; RRID:
IgG anti-mouse HRP	Cell signaling Technology	Cat#7076; RRID: AB_330924
IgG anti-rabbit HRP	Cell signaling Technology	Cat#; 7074; RRID: AB_2099233
IgG anti-mouse (Alexa 647)	Abcam	Cat#ab150119; RRID: AB_2811129
IgG anti-rabbit (Alexa 488)	Abcam	Cat#ab150081; RRID: AB_2734747
IgG Rabbit isotype control	Cell Signaling Technology	Cat#3900; RRID: AB_1550038
IgG Mouse isotype control	Cell Signaling Technology	Cat#5415; RRID: AB_10829607
Bacterial strain		
TOP10 competent *E. coli*	Thermo Fisher Scientific	Cat#C404003

Chemicals, peptides, and recombinant proteins		
UNC1999	UHN Shanghai	Cat#1431612-23-5
EPZ-6438	MedChem Express	Cat#HY-13803
CB-839	EMD Millipore	Cat#5.33717.0001
Blasticidine	Wisent	Cat#400-190-EM
Puromycin	Wisent	Cat#400-160-EM
Cristal Violet	Sigma Aldrich	Cat#C0765
Alamar Blue	Thermo Fisher Scientific	Cat#DAL1025
Formaldehyde	Sigma Aldrich	Cat#252549
Dynabeads A	Thermo Fisher Scientific	Cat#10004D
Dynabeads G	Thermo Fisher Scientific	Cat#10002D
Spike-in antibody	Active Motif	Cat#61686
Spike-in Chromatin	Active Motif	Cat#53083
DAPI	Thermo Fisher Scientific	Cat#D1306
TPE-MI	MedChem Express	Cat#HY-143218
SensiFast SYBR	Bioline	Cat#BIO-98020
siLenFect lipid reagent	Bio-rad	Cat#1703361
L-Glutamine-^{13}C5	Sigma Aldrich	Cat#605166, CAS: 184161-19-1
Matrigel	Corning	Cat#354248
DMEM	Gibco	Cat#11995-065
Ham's F-12	Gibco	Cat#11765-054
Penicillin–Streptomycin	Wisent	Cat#098-150
FBS dialyzed	Wisent	Cat#080-950
EGF	BPS Bioscience	Cat# 90201-1
Insulin	Gibco	Cat#12585014
Hydrocortisone	Multicell	Cat#511-012
Rock inhibitor	Enzo Life Sciences	Cat#Y-27632
Cholera toxin	Sigma Aldrich	Cat#C8052
Gentamycin	Gibco	Cat#**15-710-072**
Kit		
Perm/Fix	BD Biosciences	Cat#554723
Seahorse FluxPaks	Agilent	Cat#103022-100
Monarch Genomic DNA purification kit	New England BioLabs	Cat#T3010S
RNeasy Fibrous Tissue Mini Kit	Qiagen	Cat#74704
RNeasy Mini Kit	Qiagen	Cat#74104
SensiFast SYBR No-ROX kit	FroggaBio	Cat#BIO-98020
Experimental models: Cell lines and models		
Human: Hs 578T	ATCC	*RRID:CVCL_0332*
Human: MDA-MB-436	ATCC	*RRID:CVCL_0623*
Human: MDA-MB-436 sgControl	This study	N/A
Human: MDA-MB-436 sgEZH2-1	This study	N/A
Human: MDA-MB-436 sgEZH2-1	This study	N/A

Human : Hs 578T sgControl	This study	N/A
Human : Hs 578T sgEZH2-2	This study	N/A
Human: HEK293T	ATCC	RRID:CVCL_0063
Human: PDC1915 (derived from GCRC1915 human tumor)	Savage et al.[62]	N/A
Human: GCRC1915	Savage et al.[62]	N/A
Human: GCRC1939	Savage et al.[62]	N/A
Mouse: NOD.Cg-PrkdcscidIl2rgtm1Wjl/SzJ	The Jackson Laboratory	Cat#JAX:005557
Recombinant DNA and RNA material		
lentiCas9-Blast (3rd generation lentiviral production)	Addgene	Plasmid #52962
psPAX2 (2nd generation lentiviral production)	Addgene	Plasmid #12260
pVSV.G (2nd generation lentiviral production)	Addgene	Plasmid #8454
sgEZH2-1	Sigma aldrich	Sanger Arrayed Whole Genome Lentiviral CRISPR Library (ID: HS5000005721)
sgEZH2-2	Sigma aldrich	Sanger Arrayed Whole Genome Lentiviral CRISPR Library (ID: HS5000005722)
Lenti-sgRNA puro (Non targeting sgRNA)	Addgene	Plasmid #104990
si-EIF2AK4/GCN2-1	Thermo Fisher Scientific	Cat#4392420, ID: s54067
si-EIF2AK4/GCN2-2	Thermo Fisher Scientific	Cat#4392420, ID: s54068
si-EIF2AK3/PERK-1	Thermo Fisher Scientific	Cat#4392420, ID: s18101
si-EIF2AK3/PERK-2	Thermo Fisher Scientific	Cat#4392420, ID: s18103
si-EIF2AK2/PKR-1	Thermo Fisher Scientific	Cat#4392420, ID: s229500
si-EIF2AK2/PKR-2	Thermo Fisher Scientific	Cat#4392420, ID: s229501
si-EIF2A/eIF2α-1	Thermo Fisher Scientific	Cat#4392420, ID: s38345
si-EIF2A/eIF2α-2	Thermo Fisher Scientific	Cat#4392420, ID: s38346
si-ATF4-1	Thermo Fisher Scientific	Cat#4392420, ID: s1702
si-ATF4-2	Thermo Fisher Scientific	Cat#4392420, ID: s1703
si-GLS-1	Thermo Fisher Scientific	Cat#4392420, ID: s5838
si-GLS-2	Thermo Fisher Scientific	Cat#4392420, ID: s5839
Software and algorithms		
FlowJo (v10.10)	Treestar	https://www.flowjo.com/
ImageJ (v2.14)	NIH	https://imagej.net/software/fiji/
Prism (v9.1.1)	GraphPad	https://www.graphpad.com/
MACS (v3.0)	Github	https://github.com/macs3-project/MACS
Trimmomatic (v0.39)	Usadel Lab	http://www.usadellab.org/cms/?page=trimmomatic
bwa (v0.7.17)	Github	https://github.com/lh3/bwa
QuPath (v0.5.0)	Github	https://github.com/qupath/qupath/releases

RESOURCE AVAILABILITY

Lead contact. Further information and requests for reagents should be directed to the lead contact, Geneviève Deblois (genevieve.deblois@umontreal.ca).

EXPERIMENTAL MODEL AND STUDY PARTICIPANT DETAILS

Cell culture. TNBC PDX-derived cell line (GCRC1915 PDC) and two established TNBC cell lines Hs 578T and MDA-MB-436 were used and maintained in a humidified 37 °C, 5% CO_2 incubator. Hs 578T and MDA-MB-436 breast cancer cells were cultured in Dulbecco's Minimal Eagle's Medium (DMEM) supplemented with 10% dialyzed fetal bovine serum (FBS) and 1% penicillin/streptomycin. The GCRC1915 PDC was cultured and maintained in Ham's F12/DMEM-media (25/75), 5% dialyzed Fetal bovine serum supplemented with 0.4µg/mL Hydrocortisone, 5µg/mL Insulin, 10ng/mL Epidermal Growth Factor, 8.4ng/mL Cholera toxin, 50µmol/mL Rock inhibitor, and 50µg/mL Gentamycin. For *in vitro* studies, cell line models were treated once with UNC1999 (1 µM), EPZ-6438 (1 µM) or CB-839 dissolved in Dimethyl Sulfoxide (DMSO).

Animal studies. All patient tissue samples used for PDXs were collected at the McGill University Health Centre and Jewish General Hospital after obtaining informed consent under REB-approved protocols and in accordance with the McGill University Health Centre research ethics board (SUR-2000-966) guidelines and the Bureau de la Conduite Responsible en Recherche (CER) from the Université de Montréal (2022-4027) per guidelines. Mice for PDXs were maintained and treated in accordance with the McGill University Health Centre research ethics board (SUR-99-780) and the Rosalind & Morris Goodman Cancer Institute of McGill University Facility Animal Care Committee (2014-7514) guidelines. TNBC patient-derived xenograft (GCRC1915 and GCRC1939) tumors were fragmented and preserved in cryotubes containing F12-DMEM supplemented with FBS and 10% DMSO at –80 °C. Fragments of 1 mm^3 were transplanted subcutaneously in the mammary fat pad of 5- to 7-week-old non-obese diabetic scid gamma (NSG) female mice. For the cellular xenograft, the Hs 578T model was transplanted in the mammary fat pad of 5- to 7-week-old non-obese diabetic scid gamma (NSG) female mice, using 7.5×10^5 cells in a 1:1 cells to Matrigel ratio. When tumors reached a volume of 150 mm^3, xenografted mice were randomly treated with either control vehicle, UNC1999 (150-300 mg/kg, 5x/week) alone, CB-839 alone (EMD Millipore; 200 mg/kg, daily) or the combination of both compounds. Tumor average

size was calculated using the formula (length x width^2)/2 using electronic calipers. Mice were terminated and tumors were collected after reaching a volume of 2000-2500 mm^3. For *in vivo* studies, UNC1999 and CB-839 were dissolved in Sodium carboxymethyl cellulose (NaCMC) and (2-Hydroxypropyl)-β-cyclodextrin (HP-β-CD), respectively, with Tween 80.

METHOD DETAILS

RNA Extraction and Sequencing. PDX samples were collected after 21 days of treatment with or without UNC1999. RNA was extracted using the RNeasy Fibrous Tissue Mini Kit (Qiagen) according to the manufacturer's protocol. Hs 578T and MDA-MB-436 cell lines were maintained as described and treated with DMSO, UNC1999, EPZ-6438, or siRNA against *ATF4* for 4 days. Cells were subjected to RNA extraction with the RNeasy Mini Kit (Qiagen) according to the manufacturer's protocol. All RNA samples were quantified using Qubit 2.0 fluorometer (Thermo Scientific) and their quality was assessed with an Agilent 2100 Bioanalyzer (Agilent Technologies). Poly-A-enriched RNA and ribo-depleted RNA libraries were generated using the KAPA RNA HyperPrep kit (Roche). Sequencing was performed on the Illumina NextSeq500 (single-end, 84bp or 74bp) or on the Illumina Novaseq (paired-end, 100bp reads). For RNA-Seq analysis, adapter sequences were trimmed using Trimmomatic (v0.35). Filtered reads were aligned to a hybrid genome formed of the reference human genome version GRCh38 (gene annotation from Gencode version 37, based on Ensembl 103) and the mouse genome version GRCm38 (Gencode version M25) using STAR version 2.7.1a. DESeq2 (v1.30.1) was used to normalize human gene read counts and compute differential expression between the various experimental conditions. Significant gene sets were chosen according to a false discovery rate (FDR), cut-off of 5% (padj < 0.05). Normalized DESeq2 read counts were also used to perform functional analysis using GSEA, such as hallmark and GO biological pathway gene sets.

Protein Extraction and Immunoblotting Analysis. Whole cell pellets were homogenized using a lysis buffer containing three detergents (Tris-HCl pH 7.5 50 mM, NaCl 150 mM, TritonX100 1%, SDS 0.1%, Sodium Deoxycholate 0.5%), sonicated (QSonica Q700, 4°C, 80% amplitude, 10 cycles 30 seconds ON/30 seconds OFF) and quantified using a Lowry assay (BioRad). Proteins (20-40 µg) were electrophorated on an 8-12% SDS-polyacrylamide gel (110V). Proteins were transferred on a PVDF membrane using a Trans-Blot Turbo Transfer System according to the

manufacturer's protocol (BioRad, Standard protocol, 30 minutes). Membranes were blocked using TBS-T (TBS 1X supplemented with Tween 20 0.05%) with 5% milk or 3% BSA for 1 hour and blotted overnight at 4 °C. Horseradish peroxidase–conjugated (HRP) secondary anti-mouse and anti-rabbit IgG were used for 45 minutes to allow immunodetection using Clarity Western ECL substrate (BioRad) for enhanced chemiluminescence (PerkinElmer Life and Analytical Sciences).

siRNA Transfection. Cells were seeded and transfected 4 hours later with siRNA (20 nM) using the siLentFect lipid reagent (BioRad) according to the manufacture's protocol for a total duration of 48-72 hours. 2 siRNAs/gene were used against *EIF2A2*/PKR, *EIF2A3*/PERK, *EIF2A4*/GCN2, *EIF2A*/eIF2α, *ATF4*, and non-Targeting siRNA ("si-Control" 1 and 2) were used as a negative control.

Lentivirus preparation and generation of stable cell lines. MDA-MB-436 and Hs 578T *EZH2* knock-out cells were generated by lentiviral transduction using different vectors expressing Cas9 (lentiCas9-Blast) and 2 different sgRNAs against *EZH2* (sg*EZH2*-1: 5'-GTTGGAAAATCCAAGTCACTGG-3' and sg*EZH2*-2: 5'-GGAGATGAAGTTTTAGATCAG-3 respectively targeting *EZH2* exons 4 and 5) or a non-targeting sgRNA (lenti-sgRNA puro). For lentiviral production, HEK 293T cells were cultured and transfected with psPAX2 and pVSV.G for the lentiviral packaging of all 3 sgRNA and Cas9 vectors. MDA-MB-436 and Hs 578T cells were first transduced with the lentivirus expressing the Cas9 and selected using blasticidin ([C]=10µg/mL) for 7 days. After the first selection, cells were infected separately with the 2 sg*EZH2* and non-targeting sgRNA. Both cell lines expressing the guides were selected using puromycin ([C]=1µg/mL) for another 7 days, and the depletion was confirmed by immunoblotting.

Chromatin Immunoprecipitation. Chromatin was prepared from UNC1999-treated PDX GCRC1915 tumors (300 mg/kg, 6x/week) and MDA-MB-436 cells (1 µM, 4 days) or control vehicle. Chromatin immunoprecipitation (ChIP) was performed on histone modification marks and ATF4 using 10^7 cells for MDA-MB-436 cells and 100 mg tumor. Cells or tissues were crosslinked with 1% formaldehyde for 10 minutes at room temperature. Extracted chromatin was sonicated (QSonica Q700, 4°C, 80% amplitude, 35 cycles 30 seconds ON/30 seconds OFF) to obtain global fragmentation of 400 bp. Immunoprecipitation (IP) for H3K27me3 and H3K27ac were performed using 4 µg of antibodies and 50 µg of sonicated chromatin, compared to 1 µg for

ATF4 antibody and 300 µg of sonicated chromatin. Drosophila spike-in antibody (2 µg) was used with 50 µg of chromatin for histone mark normalization. IgG isotype antibody and input were used as controls for each sample. Input and IP samples were purified on columns (New England BioLabs) according to the manufacture's protocol. Enrichment in ATF4 ChIP samples was verified by qPCR using SensiFast SYBR at specific DNA sites: ASNS sense: 5'-CAGGGATGTGGACAGCTTGA-3', ASNS antisense: 5'-CCTCGCAGGCATGATGAAAC-3', SLC7A11 sense: 5'-CGTGCTCTCAATTCTCCACCT-3', SLC7A11 antisense: 5'-CAAGCCCATGAGGAAGCTGA-3', BCAT1 sense: 5'-ACTAAGGCTGCTCCCCCA-3', BCAT1 antisense: 5'-AGTGAGCAGTGAGTGAGGCT-3', PSAT1 sense: 5'-GCGCTCCTTGCATTGATCAA-3', PSAT1 antisense: 5'-CTTCTGAGCCGAGTCGAAGC-3', Negative control 1 sense: 5'-ACAAAGGGAATAAGCAATCTGGCATA-3', Negative control 1 antisense: 5'-TCGGCTCCAACTCAACTCGTCTATGT-3', Negative control 2 sense: 5'-TGAGGCAGGCGGGTTATCA-3', Negative control 2 antisense: 5'-TGAAGTGGTCAACACCTCTGG-3'.

Purified DNA samples were quantified with Qubit reagent (Life Technologies) and processed for sequencing using DNA libraries generated with the KAPA DNA Hyperprep Kit (Roche). All samples were sequenced in paired-end (PE, 100 bp), except for the first replicate of the PDX GCRC1915 sample, which was sequenced in single-end (SE, 84 bp). For ChIP-Sequencing analysis, quality control-filtered reads were aligned to the reference assembly *Homo sapiens* (GRCh38 Gencode40), *Mus musculus* (GRCm39 GencodeM29), to discriminate human from mouse reads, and *Drosophila melanogaster* (BGDP.28) using bwa mem (v0.7.17). Only uniquely mapped and/or properly-paired reads were retained for further analysis. Redundant reads were removed using manual filtering of XA:Z and SA:Z tags with Mapping Quality < 30. Peaks were called using MACS (v3.0) with default values (FDR = $1x10^{-4}$). For H3K27me3 samples, peaks were called using the --broad flag. Bed files contain peak calls on merged reads, using the corresponding inputs as controls. BigWig files were generated using UCSC's bedGraphToBigWig tool (v396). Drosophila melanogaster spike-in reads were used for normalization. To compensate for sequencing mode differences, reads from single-end (SE) Drosophila spike-in samples were multiplied by a factor of two during normalization. For each sample, a normalization factor was computed as the ratio of its Drosophila read count to that of the sample with the fewest Drosophila reads. These factors were applied to normalize BigWig visualizations. BigWig files were

generated by computing the mean signal across replicates within each condition using Wiggletools (v1). Differential binding analysis for H3K27ac samples was performed using DiffBind with the DESeq2 method (DBA_DESEQ2). Input samples were scaled and subtracted to correct for background signal. Spike-in normalization factors, derived from Drosophila read count ratios, were applied as scaling factors. The contrast between conditions was manually defined using sample masks to specify the comparison of interest. Peaks with a log2 fold change > 1 and p-value < 0.05 were considered significantly differentially bound. For H3K27me3, peaks from individual samples were merged using bedtools merge to generate a consensus set of broad regions. Peak signals were visualized over scaled BigWig files using the reference-point method implemented in deepTools (v3.5.1). Peak annotation was performed with the ChIPseeker R package (v1.38.0) in R (v4.3.3).

Salmon Index Generation

To build the custom Salmon index used for quantification, transposable element (TE) sequences were extracted based on the RepeatMasker annotations. A BED file containing the genomic coordinates of TE loci was generated, and the corresponding sequences were retrieved from the human and mouse reference genomes using BEDTools getfasta (v2.30.0).

These TE sequences were then combined with transcriptome FASTA files from both human and mouse annotations. The final index was built using Salmon (v1.10.2) with a k-mer size of 31, keeping duplicate sequences and without clipping polyA tails. This combined index allowed accurate quantification of both species-specific transcripts and locus-specific TE insertions, and was designed to facilitate discrimination between human and mouse reads in PDX RNA-seq data.

Detection of TE Expression

Transposable element (TE) annotations were generated using RepeatMasker (v4.1.5). Annotation was performed by combining RepeatMasker with the HMMER tool (v3.3.1) and the Dfam database (v3.7). The output file from RepeatMasker in fa.out.gff format was converted to a GTF file using a script provided by the Hammell lab (https://github.com/mhammell-laboratory). Annotation was performed using the following command:

```
perl RepeatMasker -species [human/mouse] -gff -pa 32 -u -xm [fasta_genome_file] -dir [output_dir]
```

For RNA-seq data from PDX samples, human and mouse transcript annotations were merged with locus-specific human and mouse TE annotations, in order to distinguish the origin of sequencing reads (human vs. mouse, transcript vs TE). Quantification was performed at the locus level using Salmon (v1.10.2). Differential expression analysis was performed exclusively for human TE insertions using DESeq2 (v1.42.0), using a threshold of log2FoldChange > 1 and an adjusted p-value < 0.05. Insertions were filtered for those with at least three samples having a minimum of 10 reads.

TE Subfamily Enrichment Analysis

Enrichment of TE subfamilies was assessed by comparing the proportion of differentially upregulated human TE insertions across subfamilies to their proportion in the full set of annotated and analyzed TE loci. For each subfamily, insertions were classified into four categories based on two criteria: (i) whether the insertion was differentially expressed (DE) or not, and (ii) whether it belonged to the subfamily of interest or not. This comparison was performed using a two-sided Fisher's exact test implemented in R (v4.3.3), considering the total set of TE insertions annotated by RepeatMasker and included in the analysis as the background. Subfamilies were considered significantly enriched if they showed an odds ratio (OR) ≥ 2 and a p-value < 0.05.

For ChIP-seq and TE enrichment analyses, the genomic coordinates of human TE insertions were extracted from the RepeatMasker annotation. These coordinates were then intersected with the ChIP-seq peaks of interest using BEDTools intersect (v2.30.0) with -F 1 to identify TE insertions that were entirely contained within the peaks. Subfamily-level enrichment was subsequently assessed using the same statistical approach as described above.

Fixed cells immunofluorescence. Cells were plated on glass bottom dishes (MatTek Corporation) for the adequate treatment time and fixed with 100% methanol for 10 minutes, permeabilized with 0.2% Triton X100 for 5 minutes, and blocked using PBS-T (PBS 1X – Tween 20, 0.05%, 1 hour) and 3% BSA. Then, cells were incubated with anti-dsRNA primary antibody (1:100) overnight on a rotor at 4°C. Secondary goat anti-mouse antibody (1:500) coupled with Alexa647 was used for 45 min in the dark and followed by 300nM DAPI staining for nuclei visualization. Staining intensities were imaged using the Leica SP8 microscope and quantified using ImageJ. Relative

intensity was calculated by the ratio of dsRNA to DAPI intensity for 15 cells for each biological replicate compared to DMSO. An IgG was used in parallel as internal negative control.

Flow cytometry. Cells were detached using trypsin/EDTA and resuspended using flow cytometry buffer (PBS 1X complemented with FBS 1% and EDTA 5 mM). 10^6 cells per cell line were aliquoted, fixed and permeabilized (10 minutes, BD Perm/Wash™ Buffer) according to the manufacturer's protocol (BD Biosciences) and washed twice in the same buffer before being incubated with anti-dsRNA primary antibody (1:100) for 30 minutes on a rotor at 4 °C. Cells were washed twice one more and incubated with anti-mouse antibody (1:500) for another 30 minutes a rotor at 4 °C in the dark. Stained cells were washed twice and resuspended in flow cytometry buffer. Single cell intensity was measured by YETI cell analyzer and studied using the data acquisition software Everest. An IgG was used in parallel as internal negative control.

Tissue processing, immunohistochemistry and immunofluorescence and imaging. Sections (4 µm) were prepared from formalin-fixed and paraffin-embedded PDX. For immunohistochemistry, deparaffinization and antigen retrieval were performed using a Discovery XT automatic stainer (Ventana Medical Systems) following the manufacturer's protocol. Sections were incubated with primary antibodies using Bond polymer DAB refine kit (#DS9800, Leica Biosystems) according to the manufacturer's protocol on the Bond RX stainer (Leica Biosystems, Buffalo Grove, IL, USA) and counterstained with Gill hematoxylin to visualize the nuclei. Sections were scanned using the C9600 NanoZoomer System (Hamamatsu Corporation, Bridgewater, NJ, USA). NDP Scan software (version 2.2.9) was used to extract all images. For immunofluorescence, fresh cold cuts were processed for deparaffinization (xylene), dehydration (Ethanol 100%), and antigenic revelation (citrate buffer, pH 6.0) manually. After blocking, each protein was stained with primary antibodies anti-dsRNA antibody (1:50, mouse) and anti-H3K27me3 (1:100, rabbit) overnight at 4 °C. Secondary antibodies targeting rabbit (Alexa488) and mouse (Alexa647) IgGs were incubated for 2 hours before final staining of nuclei with 30nM DAPI. Stained tissue sections were then scanned using the CYTATION5 with 20X objective and images were scored using the QuPath software. Training was performed on several regions for cell identification based on DAPI intensity staining and nuclei shapes. For each cell, the ratio of mean H3K27me3 and dsRNA signal intensity to DAPI was calculated using a Python script. The average of three regions per condition was compiled and plotted with Prism.

Proliferation assays. Cells were seeded for each condition in a 96-well black plate (minimum of 3 technical replicates) at day 0 and incubated with medium containing the alamarBlue reagent (3 h, Invitrogen, 1:25) to be read on days 0, 3 and 6 at 590 nm using the Spark® multimode plate reader (Tecan Life Sciences). After each reading, relative growth was calculated as a ratio compared to day 0 for each condition.

Viability assays. Cells were plated in a 96-well transparent plate (3 technical replicates). After desired treatment time, cells were fixed using 100% cold-methanol for 10 minutes and stained with Crystal violet. Viability was analysed by lysing whole stained cells with 0.2% SDS and measured at 592 nm with the Spark® multimode plate reader (Tecan Life Sciences).

Protein misfolding assays. Misfolded and unfolded protein levels were measured using the tetraphenyl ethene maleimide (TPE-MI) probe emitting fluorescence upon binding to free cysteines. Cells were seeded in a 24-well black plate and treated or not with EZH2 inhibitors for 48 hours. Then, cells were incubated with TPE-MI (MedChem Express; 25 μM) for 45 minutes before analysis. After washes with 1X PBS, misfolded protein levels were quantified by measuring a fluorescence intensity at 470 nM using the Spark® multimode microplate reader (Tecan Life Sciences) and imaged by the BioTek CYTATION5 (Agilent) using the bright phase contrast and GFP channels.

Extracellular metabolite consumption rate. Hs 578T and MDA-MB-436 cells were seeded for 4 independent biological replicates and cultured with or without UNC1999 and EPZ-6438 to measure glucose, lactate, glutamine and glutamate levels in the extracellular medium. After 3 days, 1.5 mL of media was collected for each sample and corresponding cells were counted for normalization. Samples were centrifuged to remove aggregates, transferred into low binding tubes and submitted for analysis to the BioProfile 400 Analyzer (Nova Biomedical) to measure glucose (g/L), lactate (g/L), glutamine (mmol/L) and glutamate (mmol/L) concentrations. Metabolite concentrations from the naïve media were subtracted from the metabolite concentrations of the samples to obtain the relative uptake or release and normalized by the number of cells to compare treated to untreated conditions.

Metabolite extraction for LC-MS. Both Hs 578T and MDA-MB-436 were maintained as described and treated with DMSO, UNC1999 or EPZ-6834 for 3 days and transfected with siControl, siATF4-1 or siATF4-2. Extracellular medium was collected for differential amino acid analysis, and in the case of tracing, cells were washed with 150 mM (pH=7.4) ammonium formate buffer containing N-ethylmaleimide (NEM) to protect thiols, harvested with 50% MeOH/50% LC/MS-grade water (with NEM). To both sample types, acetonitrile (ACN) was added and cells homogenized by bead beating. Lastly, the samples were partitioned using dichloromethane and water. Polar (aqueous layer) metabolites were dried in a sample cooled (-4ºC) vacuum concentrator overnight. The samples were stored at −80°C until further analysis was performed.

LC-MS. For the detection of central carbon metabolites two chromatographic methods were employed using Agilent 6470 Triple Quadrupole (QQQ) instruments for targeted multiple reaction monitoring (MRM) while quadrupole time of flight (Agilent 6530 and 6545) instruments were used for stable isotope tracer analyses. Chromatography was achieved using a 1290 Infinity ultra-high performance LC system (Agilent Technologies, Santa Clara, CA, USA). The mass spectrometers are equipped with a Jet Stream electrospray ionization (ESI) source. For all LC-MS analyses, 5 µL of the sample was injected. Data were analyzed using MassHunter Quant (Agilent Technologies) for steady state analysis and Profinder (Agilent Technologies) for stable isotope tracer analysis. No additional corrections were made for ion suppression. For both LC/MS analyses, the peak intensity (integrated peak area) of each metabolite was identified to calculate its relative abundance compared to the medium only (naïve medium). The values were normalized using the total sum of peak area for all metabolites analyzed for each sample, and differential enrichment of metabolites was calculated for drug and siRNA treatment using fold change and logarithmic analysis. Further statistical analyses were also done using Metaboanalyst online tools.

Ion pairing method. Samples were analyzed in negative mode. Multiple reaction monitoring was optimized on authentic metabolite standards. Source gas temperature and flow were set at 150°C and 13 L/min, respectively, nebulizer pressure was set at 45 psi, and capillary voltage was set at 2000V. The autosampler temperature was maintained at 4°C. Metabolite separation was achieved by using a Zorbax Extend C18 column 1.8 µm, 2.1 × 150mm^2 with guard column 1.8 µm, 2.1 × 5mm^2 (Agilent Technologies) maintained at 35°C. The chromatographic gradient started at 100% mobile phase A (97% water, 3% methanol, 10 mM tributylamine, 15 mM acetic acid, 5 µM

medronic acid) for 2.5-min, followed by a 5-min gradient to 20% mobile phase C (methanol, 10 mM tributylamine, 15 mM acetic acid, 5 µM medronic acid), a 5.5-min gradient to 45% C and a 7-min gradient to 99% mobile phase C, which was kept for 4 min. The column was restored by washing with 99% mobile phase D (90% ACN) for 3 min at 0.25 mL min^{-1}, followed by an increase of the flow rate to 0.8 mL min^{-1} over 0.5 min and a 3.85-min hold, after which the flow rate was reduced to 0.6 mL min^{-1} over 0.15 min. The column was then re-equilibrated at 100% A over 0.75 min, during which the flow rate was decreased to 0.4 mL min^{-1} and held for 7.65 min. One minute before the next injection, the flow was returned to 0.25 mL/min at 35°C. Retention times and linear detection range were obtained by running authentic standard mixes. Repeat injections of authentic standards were performed throughout the run to observe any retention time shifts and chromatographic quality. The areas under the curve for each sample and metabolite were analyzed to ensure they were below the saturation limit for those metabolites for which range curves were available. Samples were diluted 10-fold and re-run for analytes exceeding the linear range of the instrument.

Intrada-AA method. For better coverage of positive ionizing metabolites and amino acids which are not retained in reversed phase, we used a hydrophilic interaction chromatography. Using same parameters for gas temperature and flow, nebulizer pressure and capillary voltage, chromatographic separations of metabolites were achieved using an Intrada Amino Acid column 3 µm, 3.0×150mm (Imtakt Corp, JAPAN). The chromatographic gradient started at 100% mobile phase B (0.3% formic acid in ACN) with a 3 min gradient to 27% mobile phase A (100 mM ammonium formate in 20% ACN / 80% water) followed by a 19.5 min gradient to 100% A at a flow rate of 0.6 ml/min. This was followed by a 5.5 min hold time at 100% mobile phase A and a subsequent re- equilibration time (7 min) before the next injection. The column temperature was maintained at 10°C. Relative concentrations were determined from external calibration curves of standards dissolved in water to ensure that samples analyzed were within the linear range of the instrument. For those that exceeded the linear range 30-fold dilutions were made and samples re-analyzed. For all LC/MS analyses, 5 µL of the sample was injected. Data were analyzed using MassHunter Quant (Agilent Technologies). No additional corrections were made for ion suppression.

Stable Isotope Tracer analysis (SITA). For stable isotope tracer metabolite analysis of glutamine, Hs 578T was maintained as described and treated with DMSO or 1-2 μM UNC for 2 days. DMSO- and UNC-treated Hs 578T cells were then grown in DMEM containing 4 mM 13C5-labelled glutamine (CML-1822; Cambridge Isotope Laboratories, Inc.) or unlabelled glutamine for 2 h. Samples were collected and extracted as explained above. The same columns and chromatographic methods and source settings were used for SITA as noted above. Data were collected in high resolution scan mode on both QTOF instruments (6530 and 6545 QTOF). Retention times and linear detection range were obtained by running authentic standard mixes. Repeat injections of authentic standards were performed throughout the run to observe any shifts in retention time, interferences or chromatographic quality. The areas under the curve for each sample and metabolite and isotopes were analyzed and ensured to be below the saturation limit for those metabolites where range curves were available. Stable isotope tracer data were analyzed, and natural abundance matrix correction was performed using Profinder software (Agilent Technologies). Cells were exposed to 13C-labeled nutrients, and control samples were exposed to natural abundance nutrients to ensure that observed 13C incorporation into other metabolites is not an interfering ion.

Extracellular measurement of oxygen consumption rate. Cells were plated and treated for 72 hours with EZH2 inhibitors before analysis. Oxygen consumption and extracellular acidification rates were measured three to four times using the Seahorse Extracellular Flux (XF-96) analyzer (Seahorse Bioscience). Data were calculated and presented as OCR in pmol/min/μg of protein and ECAR in mpH/min/ μg of protein. Basal and maximal respiration were plotted as a function of cells with and without treatments under the basal condition. Sequential addition of oligomycin (1 μM, after 20 minutes), FCCP (0.5 μM, after 40 minutes) and Rotenone and antimycin A (0.5μM, after 60 minutes) as indicated allowed the measurement of the ATP production and maximal oxygen consumption after the addition of oligomycin and FCCP respectively.

QUANTIFICATION AND STATISTICAL ANALYSIS

Prism 9 (GraphPad) was used for graphical representation and statistical analysis to determine significance. Data are presented as mean ± standard deviation (SD), with no exclusions made. Statistical significance was assessed using a two-tailed Student's t-test, one-way or two-way

ANOVA with post hoc Dunnett's multiple-comparisons tests, as specified in the figure legends. All statistical analyses were conducted under the assumption of normal distribution and homogeneity of variances. Group variances were comparable. A P value of ≤ 0.05 was considered statistically significant. For all *in vivo* experiments, sample sizes were predetermined using statistical and strength methods, and blinding was implemented.

RESSOURCE AVAILABILITY

Requests for further information and resources should be directed to and will be fulfilled by the lead contact, Geneviève Deblois, Ph.D. (genevieve.deblois@umontreal.ca). Any additional information required to reanalyze the data reported in this paper is available from the lead contact upon request.

AUTHOR CONTRIBUTION

Conceptualization: G.D., M.F., L.P.; Data curation: L.P., A.S.G., S.L., G.D.; Formal analyses: A.-S.G., LP, M.F., G.D.; Funding acquisition: G.D., M.P.; Investigation: L.P., M.F., E.Q., G.A., H.P., Y.A., A.M., M.S.-A., M.D.T.R., F.G.,; Methodology: L.P., M.F., G.D., A.-S.G., S.L., D.A.; Resources: M.P., G.D., S.L., S.M.; Supervision: G.D., M.P.; Writing of original draft: G.D., M.F., L.P.; Review and editing: G.D., L.P., M.P., A.-S.G., D.A.

ACKNOWLEDGEMENTS

We would like to thank all members of the Deblois lab for technical assistance and scientific input on the manuscript. The authors wish to thank the Institute for Research in Immunology and Cancer (IRIC) Genomic platform (Raphaëlle Lambert and Salwa Haidar) for ChIP-seq and RNA-seq libraries and sequencing, Histology platform (Marianne Isaac and Melina Narlis) for IHC staining. We thank the IRIC Bioinformatics platform for providing the infrastructure and assistance with the analyses. We acknowledge the Fonds de recherche du Québec (FRQ) – secteur Santé for supporting the Institute for Research in Immunology and Cancer (IRIC), an FRQ-designated research center. Metabolomics data were collected by the Metabolomics Innovation Resource (MIR) at the Rosalind and Morris Goodman Cancer Institute, McGill University. MIR is supported by our cost-recovery program, as well as the Terry Fox Research Institute, the Fondation du Cancer du sein du Québec, the Goodman Cancer Institute, and McGill University. (https://www.mcgill.ca/gci/facilities/metabolomics-innovation-resource-mir). This study was conducted with the support of the Canadian Institute for Health Research (CIHR) Funding Reference Number PJT-470501-CPT-CFCA-172840 (to G.D), the Réseau de Recherche en Cancer of the FRQ (to M. Park), Québec Breast Cancer Foundation (to M. Park) and the National Sciences and Engineering Research Councial of Canada (to S.M.). G. Deblois is a recipient of a CIHR Early Career Investigator in Cancer award, a Forbeck Scholar and a Research Scholar – Junior2 recipient from the Fonds de Recherche en Santé du Québec. M. Park is a James McGill Professor and holds the Diane and Sal Guerra Chair in Cancer Genetics at McGill University. L.P. M.F. and G.A. are recipients of a Fonds de Recherche en Santé du Québec doctoral scholarship. M.F. is a recipient of a CIHR doctoral studentship and a Canderel Doctoral Scholarship. A-S.G. and Y.A are recipients of a Fonds de Recherche en Santé du Québec Master's scholarship, a CIHR BESC-M Master scholarship, and a Centennial scholarship from the Faculty of Pharmacy of the Université de Montréal.

DECLARATION OF INTERESTS

The authors declare no competing interests.

REFERENCES

1. Kim, J., Lee, H., Yi, S.-J. & Kim, K. Gene regulation by histone-modifying enzymes under hypoxic conditions: a focus on histone methylation and acetylation. *Exp. Mol. Med.* **54**, 878–889 (2022).
2. Jo, C. *et al.* Histone acylation marks respond to metabolic perturbations and enable cellular adaptation. *Exp. Mol. Med.* **52**, 2005–2019 (2020).
3. Su, Y. *et al.* Epigenetic reprogramming of epithelial mesenchymal transition in triple negative breast cancer cells with DNA methyltransferase and histone deacetylase inhibitors. *J. Exp. Clin. Cancer Res.* **37**, 314 (2018).
4. Ratnam, N. M. *et al.* Reversing epigenetic gene silencing to overcome immune evasion in CNS malignancies. *Front. Oncol.* **11**, 719091 (2021).
5. Verma, A. *et al.* EZH2-H3K27me3 mediated KRT14 upregulation promotes TNBC peritoneal metastasis. *Nat. Commun.* **13**, 7344 (2022).
6. Pineda, B. *et al.* DNA methylation as an epigenetic signature predictive of response to neodjuvant treatment in TNBC patients. *J. Clin. Oncol.* **36**, e12658–e12658 (2018).
7. Deblois, G. *et al.* Epigenetic Switch-Induced Viral Mimicry Evasion in Chemotherapy-Resistant Breast Cancer. *Cancer Discov.* **10**, 1312–1329 (2020).
8. Marsolier, J. *et al.* H3K27me3 conditions chemotolerance in triple-negative breast cancer. *Nat. Genet.* **54**, 459–468 (2022).
9. Comet, I., Riising, E. M., Leblanc, B. & Helin, K. Maintaining cell identity: PRC2-mediated regulation of transcription and cancer. *Nat. Rev. Cancer* **16**, 803–810 (2016).
10. Lavarone, E., Barbieri, C. M. & Pasini, D. Dissecting the role of H3K27 acetylation and methylation in PRC2 mediated control of cellular identity. *Nat. Commun.* **10**, 1679 (2019).
11. Chase, A. & Cross, N. C. P. Aberrations of EZH2 in cancer. *Clin. Cancer Res.* **17**, 2613–2618 (2011).
12. Erokhin, M. *et al.* Clinical correlations of Polycomb repressive complex 2 in different tumor types. *Cancers (Basel)* **13**, 3155 (2021).
13. Parreno, V. *et al.* Transient loss of Polycomb components induces an epigenetic cancer fate. *Nature* **629**, 688–696 (2024).
14. Li, H., Cai, Q., Godwin, A. K. & Zhang, R. Enhancer of zeste homolog 2 promotes the proliferation and invasion of epithelial ovarian cancer cells. *Mol. Cancer Res.* **8**, 1610–1618 (2010).
15. Bachmann, I. M. *et al.* EZH2 expression is associated with high proliferation rate and aggressive tumor subgroups in cutaneous melanoma and cancers of the endometrium, prostate, and breast. *J. Clin. Oncol.* **24**, 268–273 (2006).
16. Morin, R. D. *et al.* Somatic mutations altering EZH2 (Tyr641) in follicular and diffuse large B-cell lymphomas of germinal-center origin. *Nat. Genet.* **42**, 181–185 (2010).

17. Gu, Z. *et al.* Loss of EZH2 Reprograms BCAA Metabolism to Drive Leukemic Transformation. *Cancer Discov.* **9**, 1228–1247 (2019).

18. Ernst, T. *et al.* Inactivating mutations of the histone methyltransferase gene EZH2 in myeloid disorders. *Nat. Genet.* **42**, 722–726 (2010).

19. Zeng, D., Liu, M. & Pan, J. Blocking EZH2 methylation transferase activity by GSK126 decreases stem cell-like myeloma cells. *Oncotarget* **8**, 3396–3411 (2017).

20. Daisuke, S. *et al.* EZH2 inhibitor DZNep induces apoptosis in adult T-cell leukemia/lymphoma cells by BCL2 suppression via regulation of Mir-181a. *Blood* **122**, 4265–4265 (2013).

21. Caganova, M. *et al.* Germinal center dysregulation by histone methyltransferase EZH2 promotes lymphomagenesis. *J. Clin. Invest.* **123**, 5009–5022 (2013).

22. Hoy, S. M. Tazemetostat: First Approval. *Drugs* **80**, 513–521 (2020).

23. Julia, E. & Salles, G. EZH2 inhibition by tazemetostat: mechanisms of action, safety and efficacy in relapsed/refractory follicular lymphoma. *Future Oncol.* **17**, 2127–2140 (2021).

24. Keller, P. J. *et al.* Comprehensive target engagement by the EZH2 inhibitor tulmimetostat allows for targeting of ARID1A mutant cancers. *Cancer Res.* **84**, 2501–2517 (2024).

25. Huang, R., Wu, Y. & Zou, Z. Combining EZH2 inhibitors with other therapies for solid tumors: more choices for better effects. *Epigenomics* **14**, 1449–1464 (2022).

26. Piunti, A. *et al.* Immune activation is essential for the antitumor activity of EZH2 inhibition in urothelial carcinoma. *Sci. Adv.* **8**, eabo8043 (2022).

27. Chibaya, L. *et al.* EZH2 inhibition remodels the inflammatory senescence-associated secretory phenotype to potentiate pancreatic cancer immune surveillance. *Nat. Cancer* **4**, 872–892 (2023).

28. Bowen, C. M. *et al.* Inhibition of histone methyltransferase EZH2 for immune interception of colorectal cancer in Lynch syndrome. *JCI Insight* **10**, (2025).

29. Nylund, P. *et al.* A distinct metabolic response characterizes sensitivity to EZH2 inhibition in multiple myeloma. *Cell Death Dis.* **12**, 167 (2021).

30. Nocito, M. C. *et al.* A targetable antioxidant defense mechanism to EZH2 inhibitors enhances tumor cell vulnerability to ferroptosis. *Cell Death Dis.* **16**, 291 (2025).

31. W-M Fan, T. *et al.* Metabolic reprogramming driven by EZH2 inhibition depends on cell-matrix interactions. *J. Biol. Chem.* **300**, 105485 (2024).

32. Xu, L. *et al.* Pharmacological inhibition of EZH2 combined with DNA-damaging agents interferes with the DNA damage response in MM cells. *Mol. Med. Rep.* **19**, 4249–4255 (2019).

33. Bianchini, G., Balko, J. M., Mayer, I. A., Sanders, M. E. & Gianni, L. Triple-negative breast cancer: challenges and opportunities of a heterogeneous disease. *Nat. Rev. Clin. Oncol.* **13**, 674–690 (2016).

34. Yomtoubian, S. *et al.* Inhibition of EZH2 Catalytic Activity Selectively Targets a Metastatic Subpopulation in Triple-Negative Breast Cancer. *Cell Rep.* **30**, 755-770.e6 (2020).

35. De Brot, M., Rocha, R. M., Soares, F. A. & Gobbi, H. Prognostic impact of the cancer stem cell related markers ALDH1 and EZH2 in triple negative and basal-like breast cancers. *Pathology* **44**, 303–312 (2012).

36. Yu, Y. *et al.* Epigenetic Co-Deregulation of EZH2/TET1 is a Senescence-Countering, Actionable Vulnerability in Triple-Negative Breast Cancer. *Theranostics* **9**, 761–777 (2019).

37. Huang, X. *et al.* Targeting Epigenetic Crosstalk as a Therapeutic Strategy for EZH2-Aberrant Solid Tumors. *Cell* **175**, 186-199.e19 (2018).

38. Yamagishi, M. *et al.* Mechanisms of action and resistance in histone methylation-targeted therapy. *Nature* **627**, 221–228 (2024).

39. Tameire, F. *et al.* ATF4 couples MYC-dependent translational activity to bioenergetic demands during tumour progression. *Nat. Cell Biol.* **21**, 889–899 (2019).

40. Bai, Y. *et al.* Inhibition of enhancer of zeste homolog 2 (EZH2) overcomes enzalutamide resistance in castration-resistant prostate cancer. *J. Biol. Chem.* **294**, 9911–9923 (2019).

41. Luo, C. *et al.* H3K27me3-mediated PGC1α gene silencing promotes melanoma invasion through WNT5A and YAP. *J. Clin. Invest.* **130**, 853–862 (2020).

42. Deb, G., Thakur, V. S. & Gupta, S. Multifaceted role of EZH2 in breast and prostate tumorigenesis: epigenetics and beyond. *Epigenetics* **8**, 464–476 (2013).

43. Mahara, S. *et al.* HIFI-α activation underlies a functional switch in the paradoxical role of Ezh2/PRC2 in breast cancer. *Proc. Natl. Acad. Sci. U. S. A.* **113**, E3735-44 (2016).

44. da Hora, C. C. *et al.* Sustained NF-κB-STAT3 signaling promotes resistance to Smac mimetics in Glioma stem-like cells but creates a vulnerability to EZH2 inhibition. *Cell Death Discov.* **5**, 72 (2019).

45. Dann, S. G. *et al.* Reciprocal regulation of amino acid import and epigenetic state through Lat1 and EZH2. *EMBO J.* **34**, 1773–1785 (2015).

46. Anwar, T., Gonzalez, M. E. & Kleer, C. G. Noncanonical Functions of the Polycomb Group Protein EZH2 in Breast Cancer. *Am. J. Pathol.* (2021) doi:10.1016/j.ajpath.2021.01.013.

47. Knutson, S. K. *et al.* A selective inhibitor of EZH2 blocks H3K27 methylation and kills mutant lymphoma cells. *Nat. Chem. Biol.* **8**, 890–896 (2012).

48. Kazansky, Y. *et al.* Overcoming clinical resistance to EZH2 inhibition using rational epigenetic combination therapy. *Cancer Discov.* **14**, 965–981 (2024).

49. Lue, J. K. *et al.* Precision targeting with EZH2 and HDAC inhibitors in epigenetically dysregulated lymphomas. *Clin. Cancer Res.* **25**, 5271–5283 (2019).

50. Li, Z. *et al.* Methylation of EZH2 by PRMT1 regulates its stability and promotes breast cancer metastasis. *Cell Death Differ.* **27**, 3226–3242 (2020).

51. Zhang, L. *et al.* DNMT and EZH2 inhibitors synergize to activate therapeutic targets in hepatocellular carcinoma. *Cancer Lett.* **548**, 215899 (2022).

52. Hsieh, Y.-Y., Lo, H.-L. & Yang, P.-M. EZH2 inhibitors transcriptionally upregulate cytotoxic autophagy and cytoprotective unfolded protein response in human colorectal cancer cells. *Am. J. Cancer Res.* **6**, 1661–1680 (2016).

53. Lee, E.-S., Yoon, C.-H., Kim, Y.-S. & Bae, Y.-S. The double-strand RNA-dependent protein kinase PKR plays a significant role in a sustained ER stress-induced apoptosis. *FEBS Lett.* **581**, 4325–4332 (2007).

54. Walter, M., Teissandier, A., Pérez-Palacios, R. & Bourc'his, D. An epigenetic switch ensures transposon repression upon dynamic loss of DNA methylation in embryonic stem cells. *Elife* **5**, (2016).

55. Chomiak, A. A. *et al.* Select EZH2 inhibitors enhance viral mimicry effects of DNMT inhibition through a mechanism involving NFAT:AP-1 signaling. *Sci. Adv.* **10**, eadk4423 (2024).

56. Morel, K. L. *et al.* EZH2 inhibition activates a dsRNA-STING-interferon stress axis that potentiates response to PD-1 checkpoint blockade in prostate cancer. *Nat. Cancer* **2**, 444–456 (2021).

57. Qiu, F. *et al.* EZH2 inhibition activates dsRNA-interferon axis stress and promotes response to PD-1 checkpoint blockade in NSCLC. *J. Cancer* **13**, 2893–2904 (2022).

58. Lines, C. L., McGrath, M. J., Dorwart, T. & Conn, C. S. The integrated stress response in cancer progression: a force for plasticity and resistance. *Front. Oncol.* **13**, 1206561 (2023).

59. Wortel, I. M. N., van der Meer, L. T., Kilberg, M. S. & van Leeuwen, F. N. Surviving stress: Modulation of ATF4-mediated stress responses in normal and malignant cells. *Trends Endocrinol. Metab.* **28**, 794–806 (2017).

60. Matsumoto, H. *et al.* Selection of autophagy or apoptosis in cells exposed to ER-stress depends on ATF4 expression pattern with or without CHOP expression. *Biol. Open* **2**, 1084–1090 (2013).

61. Harding, J. J. *et al.* A phase I dose-escalation and expansion study of telaglenastat in patients with advanced or metastatic solid tumors. *Clinical cancer research: an official journal of the American Association for Cancer Research* vol. 27 4994–5003 (2021).

62. Savage, P. *et al.* Chemogenomic profiling of breast cancer patient-derived xenografts reveals targetable vulnerabilities for difficult-to-treat tumors. *Commun. Biol.* **3**, 310 (2020).

FIGURE 1

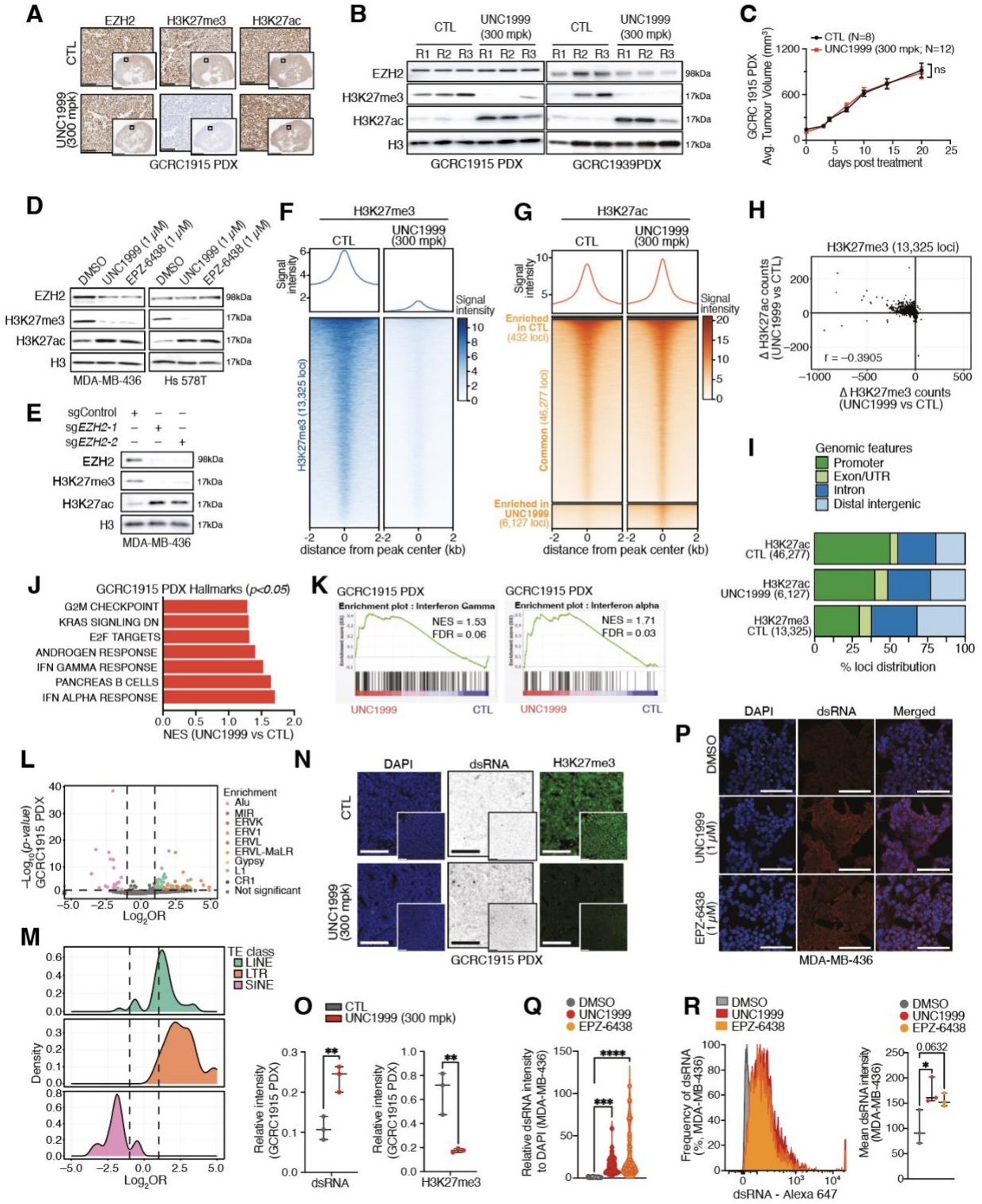
A
EZH2
H3K27me3
H3K27ac
CTL
UNC1999 (300 mpk)
GCRC1915 PDX
B
CTL
UNC1999 (300 mpk)
R1 R2 R3
EZH2
H3K27me3
H3K27ac
H3
98kDa
17kDa
GCRC1915 PDX
GCRC1939PDX
C
CTL (N=8)
UNC1999 (300 mpk; N=12)
ns
GCRC 1915 PDX Avg. Tumour Volume (mm³)
days post treatment
D
DMSO
UNC1999 (1 μM)
EPZ-6438 (1 μM)
MDA-MB-436
Hs 578T
E
sgControl
sgEZH2-1
sgEZH2-2
F
H3K27me3
Signal intensity
H3K27me3 (13,325 loci)
distance from peak center (kb)
G
H3K27ac
Enriched in CTL (432 loci)
Common (46,277 loci)
Enriched in UNC1999 (6,127 loci)
H
H3K27me3 (13,325 loci)
Δ H3K27ac counts (UNC1999 vs CTL)
Δ H3K27me3 counts (UNC1999 vs CTL)
r = −0.3905
I
Genomic features
Promoter
Exon/UTR
Intron
Distal intergenic
H3K27ac CTL (46,277)
H3K27ac UNC1999 (6,127)
H3K27me3 CTL (13,325)
% loci distribution
J
GCRC1915 PDX Hallmarks (p<0.05)
G2M CHECKPOINT
KRAS SIGNLING DN
E2F TARGETS
ANDROGEN RESPONSE
IFN GAMMA RESPONSE
PANCREAS B CELLS
IFN ALPHA RESPONSE
NES (UNC1999 vs CTL)
K
GCRC1915 PDX
Enrichment plot : Interferon Gamma
NES = 1.53
FDR = 0.06
Enrichment plot : Interferon alpha
NES = 1.71
FDR = 0.03
UNC1999
CTL
L
Enrichment
Alu
MIR
ERVK
ERV1
ERVL
ERVL-MaLR
Gypsy
L1
CR1
Not significant
−Log10(p-value) GCRC1915 PDX
Log2OR
M
TE class
LINE
LTR
SINE
Density
Log2OR
N
DAPI
dsRNA
H3K27me3
GCRC1915 PDX
O
CTL
UNC1999 (300 mpk)
Relative intensity (GCRC1915 PDX)
dsRNA
H3K27me3
P
DAPI
dsRNA
Merged
DMSO
UNC1999 (1 μM)
EPZ-6438 (1 μM)
MDA-MB-436
Q
DMSO
UNC1999
EPZ-6438
Relative dsRNA intensity to DAPI (MDA-MB-436)
R
Frequency of dsRNA (%, MDA-MB-436)
dsRNA - Alexa 647
Mean dsRNA intensity (MDA-MB-436)
0.0632

Figure 1. EZH2 Inhibition Promotes an Epigenetic Rewiring Leading to dsRNA Accumulation in TNBC. **A.** Immunohistochemistry staining of EZH2, H3K27me3 and H3K27ac on GCRC1915-PDX exposed or not to UNC1999 (300 mg/kg, 21 days, N=3). Magnification, 20X; scale bars, 100µm. **B.** Immunoblot showing the levels of EZH2, H3K27me3, H3K27ac, and total H3 in GCRC1915 and GCRC1939 PDX exposed or not to UNC1999 (300 mg/kg; 21 days; N=3). **C.** Time-dependent growth curve showing the average tumor volume of GCRC1915 PDX implanted in female NSG mice, exposed to UNC1999 (300 mg/kg; 21 days, N=12) or control (N=8). **D.** Immunoblot showing EZH2, H3K27me3, H3K27ac, and total H3 levels in MDA-MB436 and Hs 578T cells exposed to UNC1999, EPZ-6438 (1 µM, 96 h; N=3) or mock treated (DMSO, 0.2%). **E.** Immunoblot showing EZH2, H3K27me3, H3K27ac, and total H3 levels in MDA-MB436-EZH2 knock-out cells using two sgRNAs targeting EZH2 or sgControl (N=3). **F.** Left: Heatmap of peak intensity signal of H3K27me3 ChIP-seq peaks (–2 to +2 kb window) in control-treated GCRC1915 PDX (left); Right: Peak intensity of the corresponding peaks in UNC1999-treated PDX (N=3). Compilation of tag density is illustrated for the 13,325 H3K27me3 peaks at the top of each condition. **G.** Heatmap of peak intensity signal of H3K27ac (left orange) upon control or UNC1999 treatment (right) in GCRC1915 PDX. Boxes illustrate common peaks between control and UNC1999, those specific to control (N=2) or UNC1999 (N=3; >2-fold difference in peak intensity between conditions, $p<0.05$ (DiffBind)). H3K27ac tag density plots are illustrated for common and specific peaks at the top of heapmaps for each condition. **H.** Scatter plot (Pearson, p-value<0.0001) representing the difference in H3K27ac or H3K27me3 counts on H3K27me3 sites (13,325) following UNC1999 treatment in GCRC1915 PDX (300 mg/kg, 21 days; N=2-3). **I.** Stacked bar charts illustrating the proportion of H3K27me3 and H3K27ac peaks associated with distinct genomic localization/features relative to gene TSS upon control or UNC1999 treatment in GCRC1915 PDX (300 mg/kg, 21 days; N=2-3). **J.** Gene Set Enrichment Analysis (GSEA) graph representing Normalized Enrichment Score (NES) from Hallmark gene set, illustrating significantly enriched pathways ($p<0.05$) in UNC1999-treated GCRC1915 PDX relative to control treatment (300 mg/kg; 21 days; N=3). **K.** GSEA plot showing NES for interferon response alpha and gamma signaling for differentially expressed genes in response to UNC1999 (300 mg/kg; 21 days; N=3) compared to control treatment in GCRC1915 PDX. **L.** Volcano plot showing enrichment level of significantly upregulated transposable elements (TE) insertions in UNC1999-treated GCRC1915 PDX (300 mg/kg; 21 days; N=3) relative to control. Colors correspond to their

associated families. Odds ratio (OR) and p-value computed using Fisher's exact test. **M.** Density chart representing overall enrichment of TE families based on their enrichment in L. **N.** Immunofluorescence staining using J2 (dsRNA) or H3K27me3 antibodies in GCRC1915 PDX treated with control or UNC1999 (300 mg/kg; 21 days; N=3). Scale bar, 100µm. **O**. Quantification of dsRNA and H3K27me3 levels relative to DAPI intensity from **N** (N=3). **P.** Immunofluorescence staining using J2-antibody in MDA-MB436 cells exposed to DMSO (0.2%), UNC1999 or EPZ-6438 (1µM; 48 h; N=3). Scale bar, 100µm. **Q.** J2-staining quantification from **O** using Image J. **R.** Flow cytometry analysis using J2 antibody to detect dsRNA frequency in MDA-MB436 cells (Alexa 647; 1µM UNC1999; 48 h). Left: representative biological replicate. Right: mean fluorescence intensity (N=3). All data shown are mean ± SD for three biological replicates (O, Q, and R), except for tumor volume (C) where means ± SEM and N=8 (CTL) or 12 (UNC1999) are represented. Statistical analysis was performed using one-way ANOVA (Q and R) and two-tailed Student's t test (C and O). *$p < 0.05$, **$p < 0.01$, ***$p < 0.001$, ****$p < 0.0001$; ns, not significant. R: replicate #.

FIGURE 2

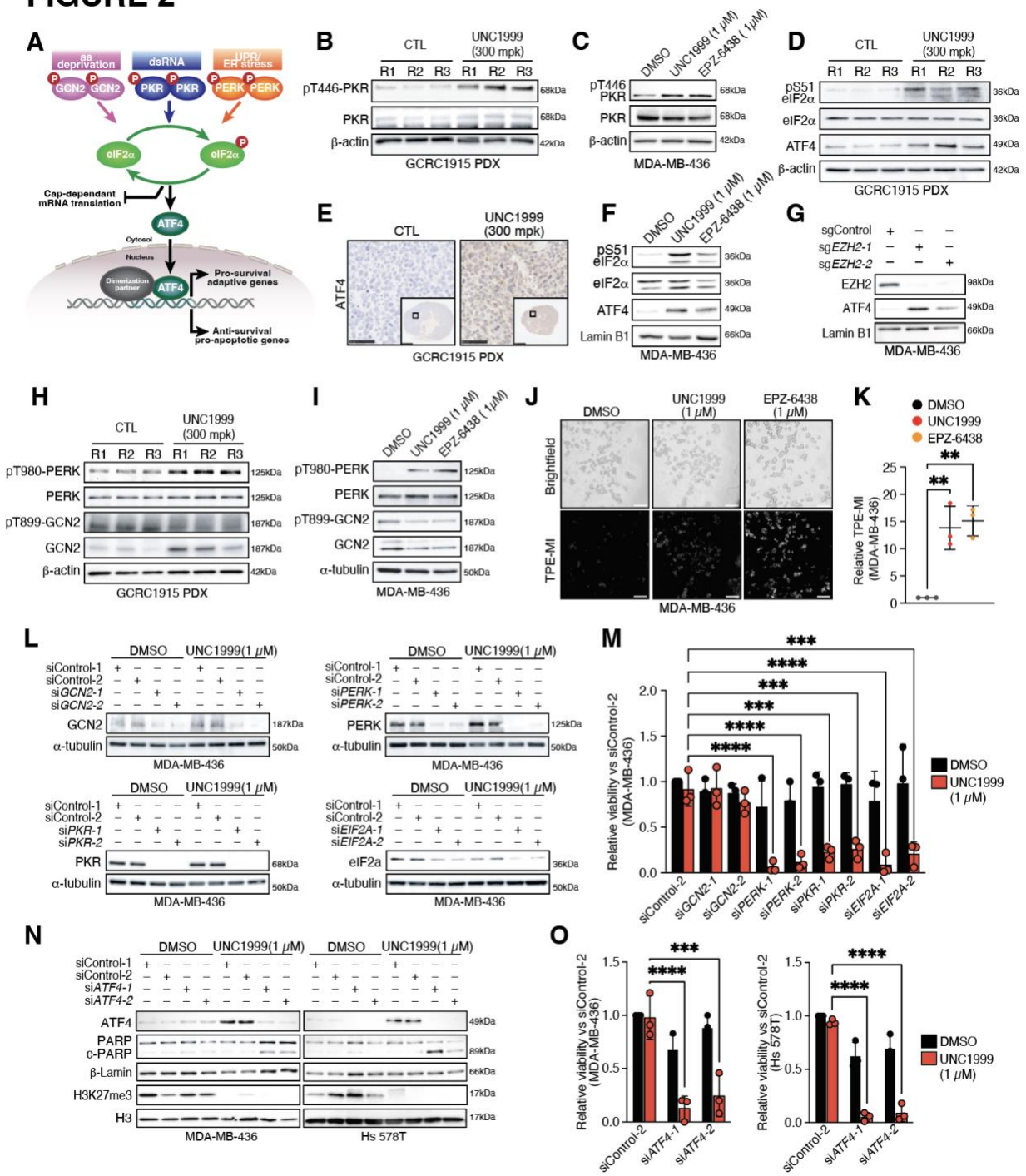
A
aa deprivation
dsRNA
UPR/ ER stress
GCN2
PKR
PERK
eIF2α
Cap-dependant mRNA translation
ATF4
Cytosol
Nucleus
Dimerization partner
Pro-survival adaptive genes
Anti-survival pro-apoptotic genes
B
CTL
UNC1999 (300 mpk)
R1 R2 R3 R1 R2 R3
pT446-PKR
PKR
β-actin
GCRC1915 PDX
C
DMSO
UNC1999 (1 μM)
EPZ-6438 (1 μM)
pT446 PKR
PKR
β-actin
MDA-MB-436
D
pS51 eIF2α
eIF2α
ATF4
β-actin
GCRC1915 PDX
E
CTL
UNC1999 (300 mpk)
ATF4
GCRC1915 PDX
F
pS51 eIF2α
eIF2α
ATF4
Lamin B1
MDA-MB-436
G
sgControl
sgEZH2-1
sgEZH2-2
EZH2
ATF4
Lamin B1
MDA-MB-436
H
pT980-PERK
PERK
pT899-GCN2
GCN2
β-actin
GCRC1915 PDX
I
pT980-PERK
PERK
pT899-GCN2
GCN2
α-tubulin
MDA-MB-436
J
DMSO
UNC1999 (1 μM)
EPZ-6438 (1 μM)
Brightfield
TPE-MI
MDA-MB-436
K
DMSO
UNC1999
EPZ-6438
Relative TPE-MI (MDA-MB-436)
L
siControl-1
siControl-2
siGCN2-1
siGCN2-2
siPERK-1
siPERK-2
siPKR-1
siPKR-2
siEIF2A-1
siEIF2A-2
GCN2
PERK
PKR
eIF2a
α-tubulin
MDA-MB-436
M
Relative viability vs siControl-2 (MDA-MB-436)
siControl-2
siGCN2-1
siGCN2-2
siPERK-1
siPERK-2
siPKR-1
siPKR-2
siEIF2A-1
siEIF2A-2
DMSO
UNC1999 (1 μM)
N
siATF4-1
siATF4-2
ATF4
PARP
c-PARP
β-Lamin
H3K27me3
H3
MDA-MB-436
Hs 578T
O
Relative viability vs siControl-2 (MDA-MB-436)
Relative viability vs siControl-2 (Hs 578T)
siControl-2
siATF4-1
siATF4-2
DMSO
UNC1999 (1 μM)

Figure 2. Induction of the Integrated Stress Response Supports TNBC Cell Survival upon EZH2 Inhibition. **A.** Schematic representing the main stresses involved in the activation of the stress kinases PKR, PERK, GCN2 that induce ISR and ISR-mediated activation of eIF2α and ATF4 induction. **B.** Immunoblot showing pT446-PKR, PKR and β-actin levels in GCRC1915 PDX exposed to control or UNC1999 treatment (300 mg/kg, 21 days; N=3). **C.** Same as in B in MDA-MB-436 cells exposed to UNC1999 or EPZ-6438 (1 μM, 48 h; N=3) or DMSO (0.2%). **D.** Immunoblot showing pS51-eIF2α, eIF2α, ATF4 and β-actin levels in GCRC1915 PDX exposed to control or UNC1999 treatment (300 mg/kg; 21 days). **E.** Immunohistochemistry staining of ATF4 on GCRC1915 PDX exposed to DMSO (0.2%) or UNC1999 (300 mg/kg, 23 days; N=3; scale bar = 50μm). **F.** Same as in D in MDA-MB-436 cells exposed to DMSO (0.2%), UNC1999 or EPZ-6438 (1 μM; 48 h, N=3). **G.** Immunoblot showing ATF4 and Lamin B1 levels in MDA-MB-436 EZH2 knock-out cells using two different sgRNAs. **H.** Immunoblot showing pT980-PERK, PERK, pT899-GCN2, GCN2 and β-actin levels in GCRC1915 PDX exposed to control or UNC1999 (300 mg/kg; 21 days; N=3). **I.** Same as in I in MDA-MB-436 cells exposed to DMSO (0.2%), UNC1999, or EPZ-6438 (1 μM; 48 h, N=3). **J.** Detection of misfolded protein load in MDA-MB-436 cells exposed to DMSO (0.2%) or EZH2 inhibitors UNC1999 or EPZ-6438 (1μM; 48 h; N=3), using the tetraphenyl ethene maleimide (TPE-MI) probe (IF). Cell density is shown in brightfield. Scale bars, 100μm. **K.** Quantification of misfolded protein load intensity from **J** showing TPE-MI intensity normalized to naïve media and relative to DMSO (0.2%). **L.** Immunoblot showing the levels of the indicated proteins (GCN2, PKR, PERK, eIF2α or αtubulin) in MDA-MB-436 cells exposed to DMSO (0.2%) or UNC1999 (1μM; 48 h, N=3) and depleted or not for the indicated protein using two siRNAs per gene (vs non-targeting siRNA (siControl)). **M.** Relative viability (crystal violet) of MDA-MB-436 cells depleted of either GCN2, PKR, PERK, or eIF2α using siRNAs (vs siControl) and exposed to UNC1999 (1μM; 96 h, N=3) or DMSO (0.2%). **N.** Immunoblot showing the levels of the indicated proteins in MDA-MB-436 and Hs 578T cells exposed to DMSO (0.2%) or UNC1999 (1μM; 72 h; N=3) and depleted of ATF4 using two siRNAs (vs siControl). **O.** Relative viability (crystal violet) of MDA-MB-436 and Hs 578T cells depleted of ATF4 using siRNAs (vs siControl) and exposed to UNC1999 (1μM; 96 h) or DMSO (0.2%; N=3). Data are the mean ± SD from 3 biological replicates (K, M, and O). Statistical analysis performed using one-way (K) and two-way ANOVA (M and O). **$p < 0.01$, ***$p < 0.001$, ****$p < 0.0001$. R: replicate #.

FIGURE 3

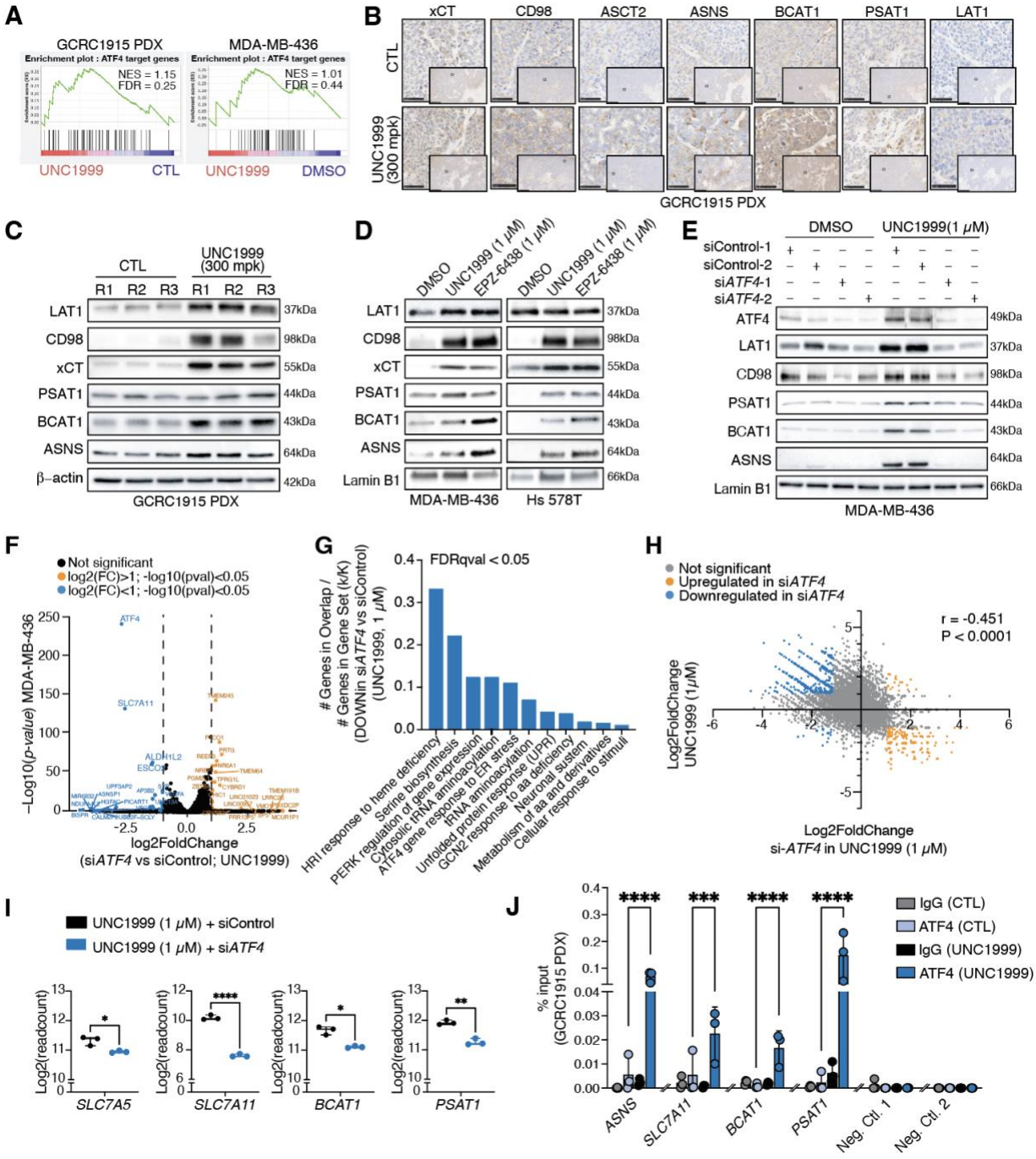
A
GCRC1915 PDX
Enrichment plot : ATF4 target genes
NES = 1.15
FDR = 0.25
UNC1999
CTL
MDA-MB-436
Enrichment plot : ATF4 target genes
NES = 1.01
FDR = 0.44
UNC1999
DMSO
B
xCT
CD98
ASCT2
ASNS
BCAT1
PSAT1
LAT1
CTL
UNC1999 (300 mpk)
GCRC1915 PDX
C
CTL
UNC1999 (300 mpk)
R1 R2 R3 R1 R2 R3
LAT1 37kDa
CD98 98kDa
xCT 55kDa
PSAT1 44kDa
BCAT1 43kDa
ASNS 64kDa
β-actin 42kDa
GCRC1915 PDX
D
DMSO
UNC1999 (1 μM)
EPZ-6438 (1 μM)
LAT1 37kDa
CD98 98kDa
xCT 55kDa
PSAT1 44kDa
BCAT1 43kDa
ASNS 64kDa
Lamin B1 66kDa
MDA-MB-436
Hs 578T
E
DMSO
UNC1999(1 μM)
siControl-1
siControl-2
siATF4-1
siATF4-2
ATF4 49kDa
LAT1 37kDa
CD98 98kDa
PSAT1 44kDa
BCAT1 43kDa
ASNS 64kDa
Lamin B1 66kDa
MDA-MB-436
F
Not significant
log2(FC)>1; -log10(pval)<0.05
log2(FC)<1; -log10(pval)<0.05
−Log10(p-value) MDA-MB-436
ATF4
SLC7A11
log2FoldChange
(siATF4 vs siControl; UNC1999)
G
FDRqval < 0.05
Genes in Overlap / # Genes in Gene Set (k/K)
(DOWNin siATF4 vs siControl)
(UNC1999, 1 μM)
HRI response to heme deficiency
Serine biosynthesis
PERK regulation of gene expression
Cytosolic tRNA aminoacylation
ATF4 gene response to ER stress
tRNA aminoacylation
Unfolded protein response (UPR)
GCN2 response to aa deficiency
Neuronal sustem
Metabolism of aa and derivatives
Cellular response to stimuli
H
Not significant
Upregulated in siATF4
Downregulated in siATF4
r = -0.451
P < 0.0001
Log2FoldChange
UNC1999 (1μM)
Log2FoldChange
si-ATF4 in UNC1999 (1 μM)
I
UNC1999 (1 μM) + siControl
UNC1999 (1 μM) + siATF4
Log2(readcount)
SLC7A5
SLC7A11
BCAT1
PSAT1
J
IgG (CTL)
ATF4 (CTL)
IgG (UNC1999)
ATF4 (UNC1999)
% input
(GCRC1915 PDX)
ASNS
SLC7A11
BCAT1
PSAT1
Neg. Ctl. 1
Neg. Ctl. 2

Figure 3. ATF4 Regulates an Amino Acid Gene Signature in Response to EZH2 Inhibition in TNBC. **A.** GSEA plot showing NES for *ATF4 targets* gene set generated from Koumenis et al.[39] in GCRC1915 PDX (left) and MDA-MB-436 (right) models exposed to UNC1999 (300 mg/kg, 21 days or 1µM, 96 h) or control (N=3). **B.** Immunohistochemistry staining of LAT1, CD98, xCT, PSAT1, BCAT1 and ASNS in GCRC1915 PDX exposed or not to UNC1999 (300 mg/kg; 21 days; N=3). Magnification, 2.5X and 40X. Scale bars, 50µm. **C.** Immunoblot showing LAT1, CD98, xCT, PSAT1, BCAT1, ASNS and β-actin levels in GCRC1915 PDX exposed to control or UNC1999 (300 mg/kg; 21 days; N=3). **D.** Same as in D in MDA-MB436 and Hs 578T cells exposed to DMSO (0.2%) or UNC1999 (1µM; 96 h; N=3). **E.** Immunoblot showing the levels of ATF4, LAT1, CD98, PSAT1, BCAT1, ASNS and Lamin B1 in MDA-MB-436 cells exposed to DMSO (0.2%) or UNC1999 (1µM; 72 h; N=3) and depleted for ATF4 using two siRNAs against *ATF4* (72 h) vs non-targeting siRNA (siControl). **F.** Volcano plots showing the -Log10(*p-value*) and the Log2 fold change in gene expression upon ATF4 depletion by siRNA (48 h) in MDA-MB-436 cells exposed to UNC1999 (1µM, 48 h, N=3). **G.** Bar graph representing up-regulated pathways (GSEA) following ATF4 depletion in MDA-MB-436 cells exposed to UNC1999 (1µM; 48 h; N=3) vs DMSO (0.2%). **H.** Scatter plot representation of Log2 fold change in gene expression resulting from UNC1999 vs DMSO (vertical) and si*ATF4* vs siControl in UNC1999-treated MDA-MB-436 cells (1µM; 48 h; N=3) (r= -0.451; p-value<0.0001). **I.** Gene expression levels of *SLC5A7*, *SLC7A11*, *PSAT1,* and *BCAT1* upon depletion of ATF4 (siATF4) vs siControl in MDA-MB-436 cells exposed to UNC1999 (1µM; 48 h; N=3). **K.** ATF4 Chromatin immunoprecipitation followed by qPCR amplification at specific ATF4 target gene promoters (*ASNS*, *SLC7A11*, *BCAT1,* and *PSAT1*) in GCRC1915 PDX exposed or not to UNC1999 (300 mg/kg; 21 days; N=3). The data presented are the mean ± SD from 3 biological replicates (I and J). Statistical analysis was performed using one-way ANOVA (J) and two-tailed Student's t test (I). *p < 0.05, **p < 0.01, ***p < 0.001, ****p < 0.0001. R: replicate #.

FIGURE 4

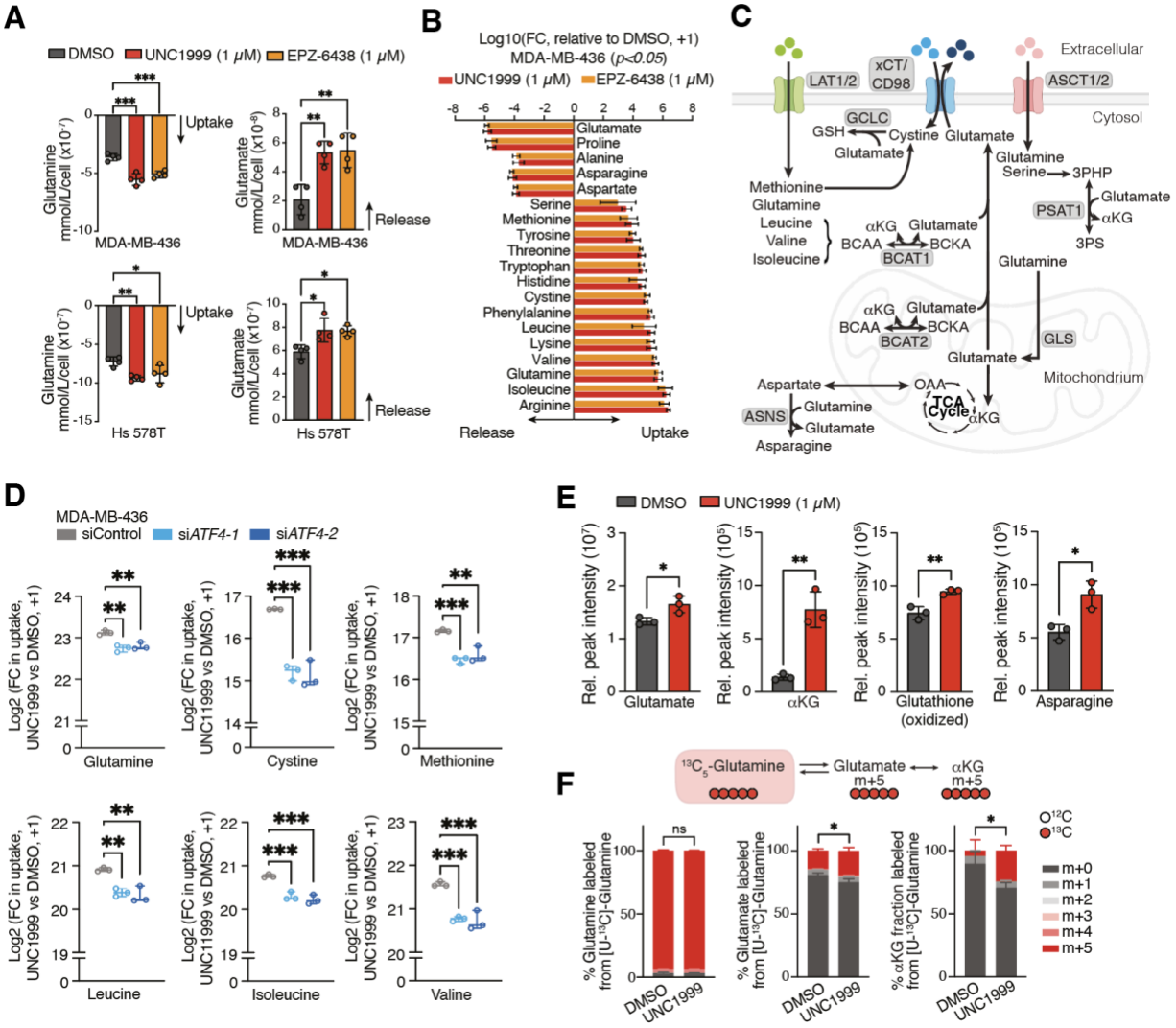
A
DMSO
UNC1999 (1 μM)
EPZ-6438 (1 μM)
Uptake
Release
Glutamine mmol/L/cell (x10⁻⁷)
Glutamate mmol/L/cell (x10⁻⁸)
MDA-MB-436
Hs 578T
B
Log10(FC, relative to DMSO, +1)
MDA-MB-436 (p<0.05)
UNC1999 (1 μM)
EPZ-6438 (1 μM)
Glutamate
Proline
Alanine
Asparagine
Aspartate
Serine
Methionine
Tyrosine
Threonine
Tryptophan
Histidine
Cystine
Phenylalanine
Leucine
Lysine
Valine
Glutamine
Isoleucine
Arginine
Release
Uptake
C
Extracellular
Cytosol
Mitochondrium
LAT1/2
xCT/ CD98
ASCT1/2
GCLC
GSH
Cystine
Glutamate
Glutamine
Serine
3PHP
PSAT1
αKG
3PS
Methionine
Leucine
Valine
Isoleucine
BCAA
BCKA
BCAT1
BCAT2
GLS
Aspartate
OAA
TCA Cycle
ASNS
Asparagine
D
MDA-MB-436
siControl
siATF4-1
siATF4-2
Log2 (FC in uptake, UNC1999 vs DMSO, +1)
Glutamine
Cystine
Methionine
Leucine
Isoleucine
Valine
E
DMSO
UNC1999 (1 μM)
Rel. peak intensity (10⁷)
Rel. peak intensity (10⁵)
Glutamate
αKG
Glutathione (oxidized)
Asparagine
F
¹³C₅-Glutamine
Glutamate m+5
αKG m+5
% Glutamine labeled from [U-¹³C]-Glutamine
% Glutamate labeled from [U-¹³C]-Glutamine
% αKG fraction labeled from [U-¹³C]-Glutamine
ns
DMSO
UNC1999
¹²C
¹³C
m+0
m+1
m+2
m+3
m+4
m+5

Figure 4. EZH2 Inhibition Induces ATF4-Mediated Metabolic Adaptation in TNBC. **A.** Relative quantification of glutamine and glutamate (BioProfile 400, Nova Biomedical) in conditioned media exposed to MDA-MB-436 or Hs 578T cells treated with UNC1999 or EPZ-6438 (1μM; 72 h) or DMSO (0.2%; N=4). **B.** Relative metabolite quantification in conditioned media using Triple Quadrupole-Liquid Chromatography-Mass Spectrometry (QQQ-LC-MS; Intrada-amino-acids) in MDA-MB-436 cells exposed to UNC1999 or EPZ-6438 ($p<0.05$; 1μM; 72 h) or DMSO (0.2%; N=4). Metabolite levels for each experimental condition are normalized to those of the naïve medium. **C.** Schematic representation of amino acid uptake and glutaminolysis coupled with transaminase reactions and antioxidant response. **D.** Relative metabolite levels in conditioned media using QQQ-LC-MS (Intrada-amino-acids) in MDA-MB-436 cells exposed to DMSO (0.2%) or UNC1999 (1μM; 60h) and transfected with non-targeting siRNA (siControl) or two siRNA against *ATF4* (20nM; 60h; N=3). Metabolite levels for each experimental condition are normalized against those of the naïve medium. **E.** Quantification of selected intracellular metabolites in Hs 578T cells using Quadrupole Time-of-Flight (QTOF)-LC-MS (Ion-pairing) exposed to UNC1999 (1μM; 72 h) or DMSO (0.2%; N=3). **F.** Stack bars illustrating stable isotope tracing analysis (SITA) using glutamine-deprived media supplemented with $^{13}C_5$-glutamine (4mM) to identify the fractional pool of labeled glutaminolysis intermediates (glutamine m+5, glutamate m+5 and αKG m+5) in Hs 578T cells exposed to DMSO (0.2%) or UNC1999 (1μM, 96 h), quantified by QTOF-LC-MS (ion pairing) after 30 minutes exposure to $^{13}C_5$-glutamine. The data shown are the mean ± SD from 3 to 4 biological replicates (A, B, D, E and F). Statistical analysis was performed by one-way ANOVA (A, B and D) and two-tailed Student's t test (E and F). *$p < 0.05$, **$p < 0.01$, ***$p < 0.001$, ****$p < 0.0001$; ns, not significant.

FIGURE 5

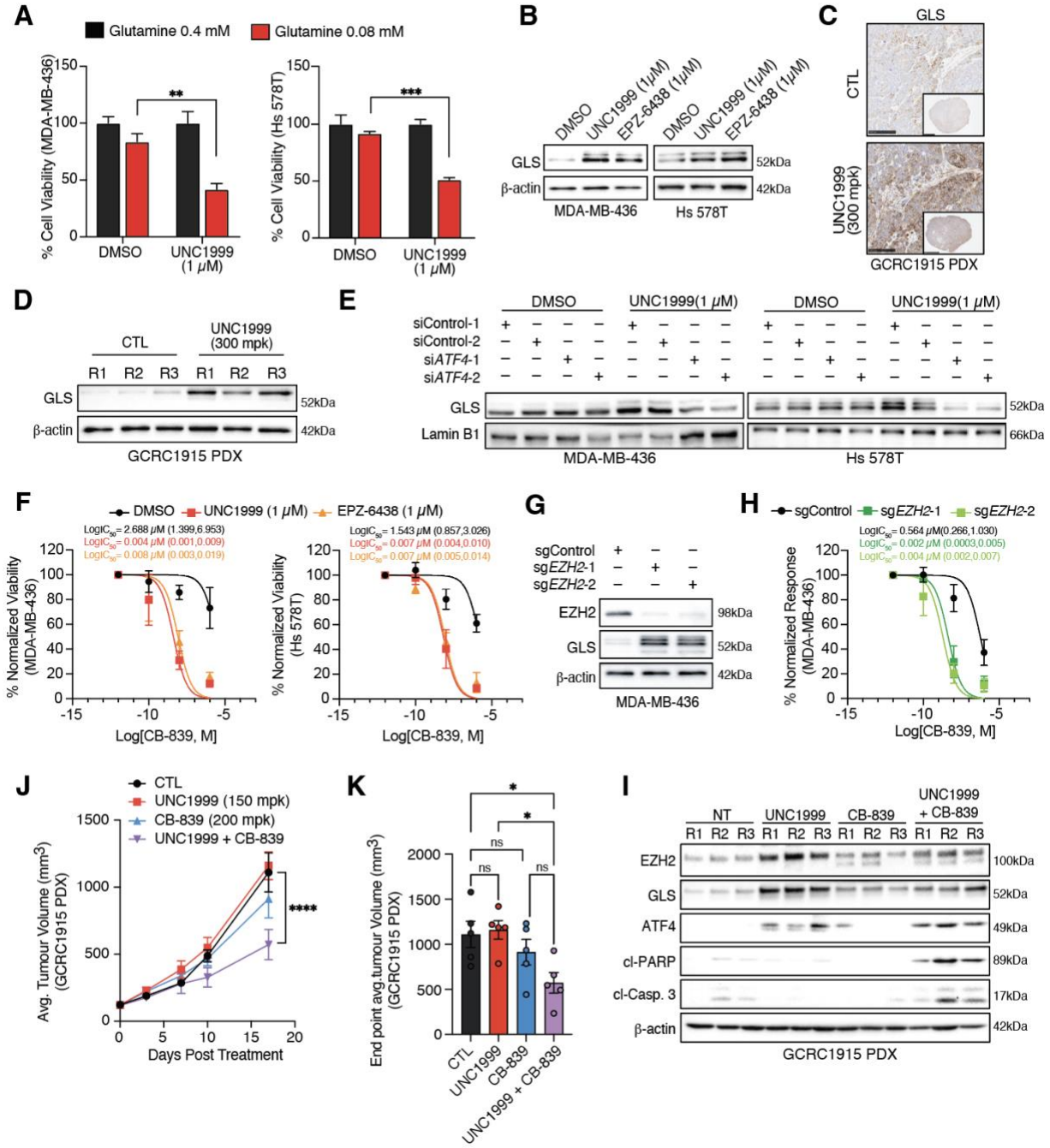
A
Glutamine 0.4 mM
Glutamine 0.08 mM
% Cell Viability (MDA-MB-436)
% Cell Viability (Hs 578T)
DMSO
UNC1999 (1 μM)
B
DMSO
UNC1999 (1μM)
EPZ-6438 (1μM)
GLS
β-actin
52kDa
42kDa
MDA-MB-436
Hs 578T
C
GLS
CTL
UNC1999 (300 mpk)
GCRC1915 PDX
D
CTL
UNC1999 (300 mpk)
R1 R2 R3 R1 R2 R3
GLS
β-actin
52kDa
42kDa
GCRC1915 PDX
E
DMSO
UNC1999(1 μM)
siControl-1
siControl-2
siATF4-1
siATF4-2
GLS
Lamin B1
52kDa
66kDa
MDA-MB-436
Hs 578T
F
DMSO
UNC1999 (1 μM)
EPZ-6438 (1 μM)
LogIC50= 2.688 μM (1.399,6.953)
LogIC50= 0.004 μM (0.001,0.009)
LogIC50= 0.008 μM (0.003,0.019)
LogIC50= 1.543 μM (0.857,3.026)
LogIC50= 0.007 μM (0.004,0.010)
LogIC50= 0.007 μM (0.005,0.014)
% Normalized Viability (MDA-MB-436)
% Normalized Viability (Hs 578T)
Log[CB-839, M]
G
sgControl
sgEZH2-1
sgEZH2-2
EZH2
GLS
β-actin
98kDa
52kDa
42kDa
MDA-MB-436
H
sgControl
sgEZH2-1
sgEZH2-2
LogIC50= 0.564 μM(0.266,1.030)
LogIC50= 0.002 μM (0.0003,0.005)
LogIC50= 0.004 μM (0.002,0.007)
% Normalized Response (MDA-MB-436)
Log[CB-839, M]
J
CTL
UNC1999 (150 mpk)
CB-839 (200 mpk)
UNC1999 + CB-839
Avg. Tumour Volume (mm3) (GCRC1915 PDX)
Days Post Treatment
****
K
ns
*
End point avg.tumour Volume (mm3) (GCRC1915 PDX)
CTL
UNC1999
CB-839
UNC1999 + CB-839
I
NT
UNC1999
CB-839
UNC1999 + CB-839
R1 R2 R3 R1 R2 R3 R1 R2 R3 R1 R2 R3
EZH2
GLS
ATF4
cl-PARP
cl-Casp. 3
β-actin
100kDa
52kDa
49kDa
89kDa
17kDa
42kDa
GCRC1915 PDX

Figure 5. Blocking glutaminase sensitizes TNBC to EZH2 inhibition. **A.** Percent viability of MDA-MB-436 (left) or Hs 578T (right) cells exposed to UNC1999 (1μM; 96 h) or DMSO (0.2%; N=3) exposed to either full media (0.4 mM glutamine) or to media depleted in glutamine (0.08 mM) (data shown relative to full media). **B.** Immunoblot showing GLS and β-actin levels in MDA-MB-436 or Hs 578T cells exposed to UNC1999, EPZ-6438 (1μM; 96 h) or DMSO (0.2%; N=3). **C.** Immuno-histochemistry (IHC) staining for GLS in GCRC1915 PDX exposed or not to UNC1999 (300 mg/kg, 21 days, N=3). Magnification, 20X; scale bars, 100μm. **D.** Immunoblot showing GLS and β-actin levels in GCRC1915 PDX exposed or not to UNC1999 (300 mg/kg; 21 days; N=3). **E.** Immunoblot showing GLS and Lamin B1 levels in MDA-MB-436 or Hs 578T cells exposed to UNC1999 (1μM; 72 h) or DMSO (0.2%; N=3) and depleted of ATF4 using two siRNAs against *ATF4* (60h) vs non-targeting siRNAs (siControl). **F.** Dose-response curves representing the relative normalized viability of MDA-MB-436 (left) and Hs 578T (right) cells exposed to DMSO (0.2%) or UNC1999 (1μM; 120h) (N=3) and co-treated with varying doses of CB-839. IC50 (95% Confidence Interval) was calculated and indicated at the top of each graph. **G.** Immunoblot showing GLS and β-actin levels in MDA-MB-436 EZH2 knock-out cells using two different sgRNAs (N=3). **H.** Dose-response curves representing the relative normalized viability of MDA-MB-436 EZH2 knock-out cells and co-treated with increasing doses of CB-839 (120 h; N=3). IC50 (95% Confidence Interval) was calculated and indicated at the top of the graph. **I.** Graph showing average tumor volume over time for GCRC1915 PDX implanted in female NSG mice and treated as indicated (control, CB-839 (200 mg/kg; 17 days), UNC1999 (150 mg/kg; 17 days) or combination) (17 days; N=5 per group). **J.** Bar graph showing average tumor volume as in J on day 17 (endpoint). **K.** Immunoblot showing EZH2, GLS, ATF4, cl-PARP, cl-Caspase3, and β-actin levels in GCRC1915 PDX tumors treated with CTL, CB-839 (200 mg/kg), UNC1999 (150 mg/kg), or combination (17 days; N=3). Data represented are means ± SD from 3 biological replicates (A, F, and H); error bars represent SEM for tumor volume (J and K). Statistical analysis was performed by one-way (K) and two-way ANOVA (J) and two-tailed Student's t test (A). *$p < 0.05$, **$p < 0.01$, ***$p < 0.001$, ****$p < 0.0001$; ns, not significant. R: replicate #.

FIGURE S1

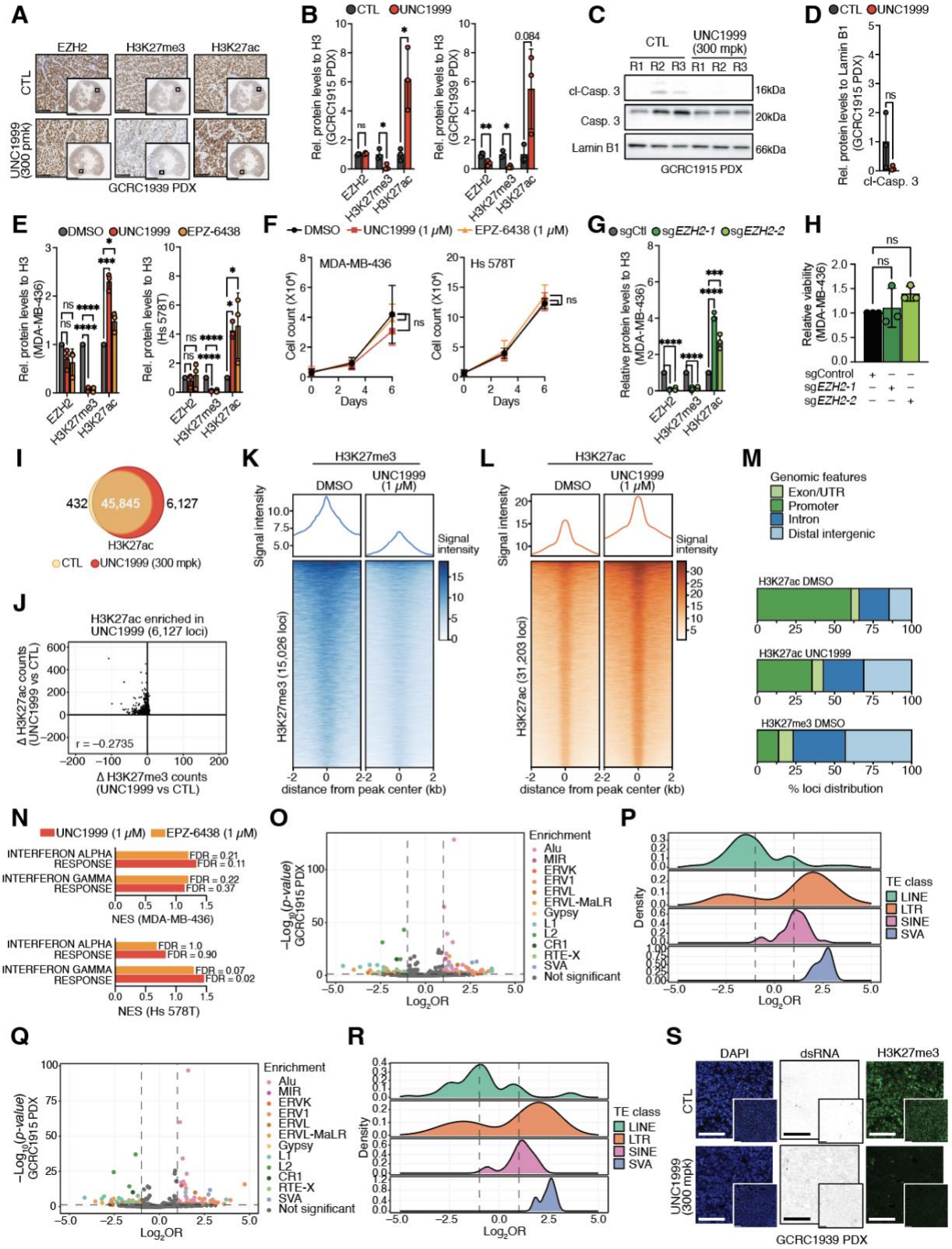
A
EZH2
H3K27me3
H3K27ac
CTL
UNC1999 (300 pmk)
GCRC1939 PDX
B
CTL UNC1999
Rel. protein levels to H3 (GCRC1915 PDX)
Rel. protein levels to H3 (GCRC1939 PDX)
ns
0.084
C
CTL
UNC1999 (300 mpk)
R1 R2 R3 R1 R2 R3
cl-Casp. 3
Casp. 3
Lamin B1
16kDa
20kDa
66kDa
GCRC1915 PDX
D
CTL UNC1999
Rel. protein levels to Lamin B1 (GCRC1915 PDX)
cl-Casp. 3
E
DMSO UNC1999 EPZ-6438
Rel. protein levels to H3 (MDA-MB-436)
Rel. protein levels to H3 (Hs 578T)
F
DMSO UNC1999 (1 μM) EPZ-6438 (1 μM)
MDA-MB-436
Hs 578T
Cell count (X10⁴)
Days
G
sgCtl sgEZH2-1 sgEZH2-2
Relative protein levels to H3 (MDA-MB-436)
H
Relative viability (MDA-MB-436)
sgControl
sgEZH2-1
sgEZH2-2
I
432
45,845
6,127
H3K27ac
CTL UNC1999 (300 mpk)
J
H3K27ac enriched in UNC1999 (6,127 loci)
Δ H3K27ac counts (UNC1999 vs CTL)
Δ H3K27me3 counts (UNC1999 vs CTL)
r = −0.2735
K
H3K27me3
DMSO
UNC1999 (1 μM)
Signal intensity
H3K27me3 (15,026 loci)
distance from peak center (kb)
L
H3K27ac
H3K27ac (31,203 loci)
M
Genomic features
Exon/UTR
Promoter
Intron
Distal intergenic
H3K27ac DMSO
H3K27ac UNC1999
H3K27me3 DMSO
% loci distribution
N
UNC1999 (1 μM) EPZ-6438 (1 μM)
INTERFERON ALPHA RESPONSE
INTERFERON GAMMA RESPONSE
FDR = 0.21
FDR = 0.11
FDR = 0.22
FDR = 0.37
NES (MDA-MB-436)
FDR = 1.0
FDR = 0.90
FDR = 0.07
FDR = 0.02
NES (Hs 578T)
O
Enrichment
Alu
MIR
ERVK
ERV1
ERVL
ERVL-MaLR
Gypsy
L1
L2
CR1
RTE-X
SVA
Not significant
−Log10(p-value) GCRC1915 PDX
Log2OR
P
TE class
LINE
LTR
SINE
SVA
Density
Q
R
S
DAPI
dsRNA
H3K27me3
CTL
UNC1999 (300 mpk)
GCRC1939 PDX

Supplementary Figure 1. A. Immunohistochemistry staining of EZH2, H3K27me3, and H3K27ac on GCRC1939 PDX exposed or not to UNC1999 (300 mg/kg, 21 days) (N=3); magnification, 20X; scale bars, 100µm. **B.** Quantification of the relative protein levels from Fig.1B (rel. to H3; N=3). **C.** Immunoblot showing cl-Caspase 3, Caspase 3 and Lamin B1 levels in GCRC1915-PDX exposed or not to UNC1999 (300 mg/kg; 21 days) (N=3). **D.** Quantification of the relative cl-Caspase 3 levels from Fig.S1C (rel. to Lamin B1; N=3). **E.** Quantification of the relative protein levels from Fig.1D (rel. to H3; N=3). **F.** Cell counts representing cell proliferation of MDA-MB-436 (left) and Hs 578T (right) cells exposed to UNC1999 or EPZ-6438 (1µM) or DMSO (0.2%) for up to 6 days (N=3). **G.** Quantification of the relative protein levels from Fig.1E (rel. to H3; N=3). **H.** Relative viability (crystal violet) of MDA-MB-436 EZH2 knock-out cells using two different sgRNAs against *EZH2* (120h) or non-targeting sgRNA (sgControl) (N=3). **I.** Venn diagrams representing the number of H3K27ac peaks that are common, specific to control, or to UNC1999 treatment (300 mg/kg, 21 days) in GCRC1915-PDX (N=2-3). **J.** Scatter plot depicting the enrichment of H3K27me3 and H3K27ac counts (UNC1999 vs Control) at the 6,127 H3K27ac peaks specifically enriched in UNC1999-treated GCRC1915 PDX (300 mg/kg, 21 days) (N=2-3) r = -0.2737; p-value<0.0001, Pearson). **K.** Heatmap of peak intensity signal of H3K27me3 ChIP-seq peaks (–2 to +2kbp window around peak center) in MDA-MB-436 cells treated with DMSO (left blue) or UNC1999 (right blue) (N=3). Compiled tag density plots are illustrated at the top of each condition. **L.** Heatmap of peak intensity signal of H3K27ac upon DMSO (0.2%; left orange) or UNC1999 (right orange) treatment in MDA-MB-436 cells (N=2). Compiled tag density plots are illustrated at the top of each condition. **M.** Bar charts illustrating the proportion of H3K27me3 and H3K27ac peaks following DMSO (0.2%) or UNC1999 treatment (1µM; 96 h) in MDA-MB436 cells and associated with genomic features relative to gene TSS (N=2-3). **N.** GSEA illustrating *Interferon alpha response* and *Interferon gamma response* from Hallmark gene set in MDA-MB-436 (up) and Hs 578T (down) cells exposed to UNC1999 (1µM, 96 h) relative to DMSO (0.2%; N=3). **O.** Volcano plot showing enrichment of TEs fully located within H3K27me3 peaks that gained H3K27ac following UNC1999 treatment in GCRC1915 PDX (N=2-3). Colors correspond to their associated families. Odds ratio (OR) and p-value computed using Fisher's exact test. **P.** Density chart representing global enrichment of TE families based on their enrichment in N. **Q.** Volcano plot showing enrichment of TEs fully located in H3K27me3 peaks in GCRC1915 PDX (N=3). Colors correspond to their associated families. Odds ratio (OR) and p-value computed

using Fisher's exact test. **R.** Density chart representing global enrichment of TE families based on their expression in P. **S.** Immunofluorescence staining using J2 or H3K27me3 antibodies in GCRC1939 PDX exposed to UNC1999 (300 mg/kg; 21 days) or control (N=3). Scale bar, 100µm. Data represent the mean ± SD from 3 biological replicates (B, D, E, F and G). Statistical analysis was performed by two-tailed Student's t test (B and D), one-way (E, G and H) and two-way ANOVA (F). ns, not significant, *$p < 0.05$, **$p < 0.01$, ***$p < 0.001$, ****$p < 0.0001$. R: replicate #.

FIGURE S2

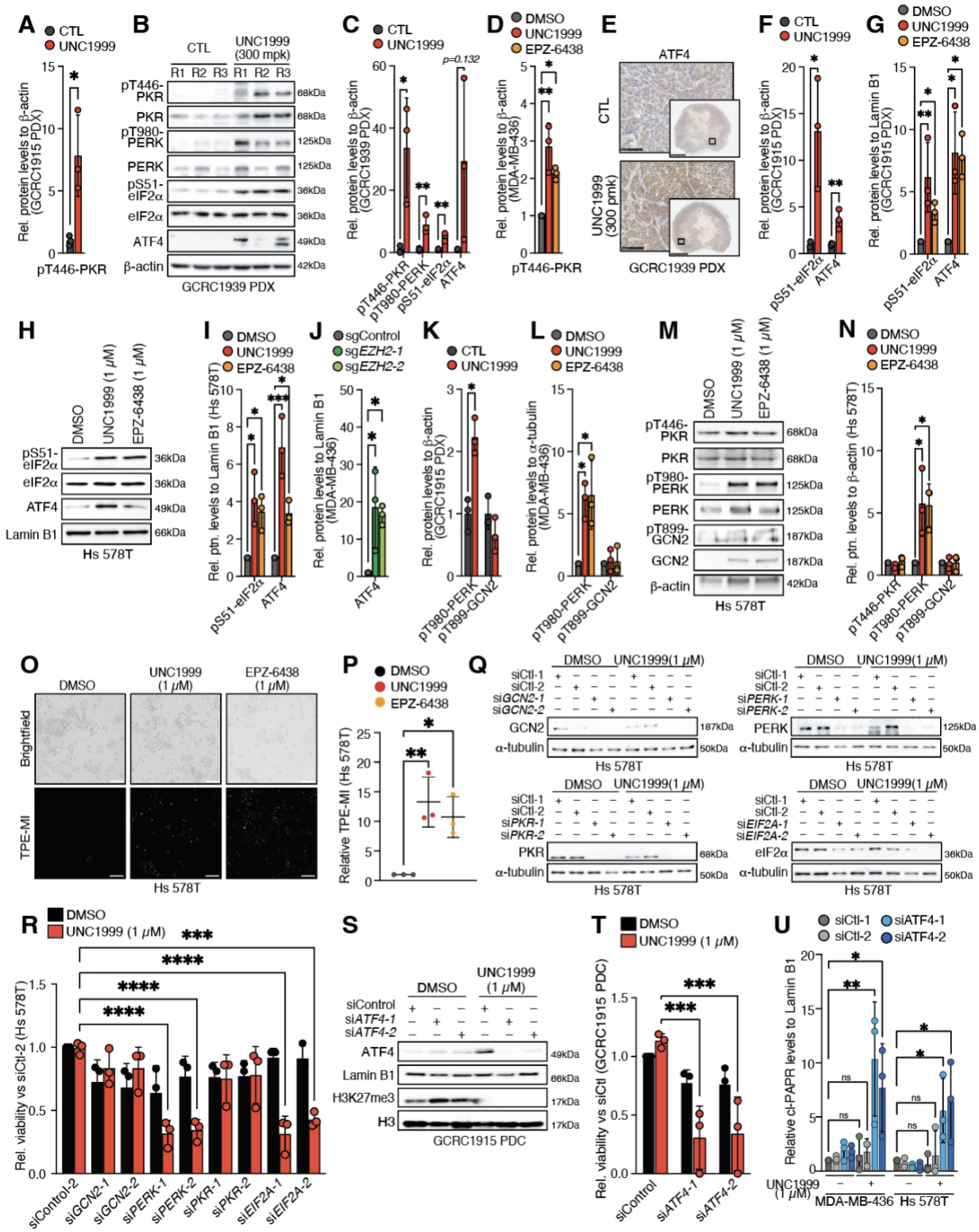
A
CTL
UNC1999
Rel. protein levels to β-actin (GCRC1915 PDX)
pT446-PKR
B
CTL
UNC1999 (300 mpk)
R1 R2 R3 R1 R2 R3
pT446-PKR
PKR
pT980-PERK
PERK
pS51-eIF2α
eIF2α
ATF4
β-actin
68kDa
125kDa
36kDa
49kDa
42kDa
GCRC1939 PDX
C
CTL
UNC1999
Rel. protein levels to β-actin (GCRC1939 PDX)
p=0.132
pT446-PKR
pT980-PERK
pS51-eIF2α
ATF4
D
DMSO
UNC1999
EPZ-6438
Rel. protein levels to β-actin (MDA-MB-436)
pT446-PKR
E
ATF4
CTL
UNC1999 (300 pmk)
GCRC1939 PDX
F
CTL
UNC1999
Rel. protein levels to β-actin (GCRC1915 PDX)
pS51-eIF2α
ATF4
G
DMSO
UNC1999
EPZ-6438
Rel. protein levels to Lamin B1 (GCRC1915 PDX)
pS51-eIF2α
ATF4
H
DMSO
UNC1999 (1 μM)
EPZ-6438 (1 μM)
pS51-eIF2α
eIF2α
ATF4
Lamin B1
36kDa
49kDa
66kDa
Hs 578T
I
DMSO
UNC1999
EPZ-6438
Rel. ptn. levels to Lamin B1 (Hs 578T)
pS51-eIF2α
ATF4
J
sgControl
sgEZH2-1
sgEZH2-2
Rel. protein levels to Lamin B1 (MDA-MB-436)
ATF4
K
CTL
UNC1999
Rel. protein levels to β-actin (GCRC1915 PDX)
pT980-PERK
pT899-GCN2
L
DMSO
UNC1999
EPZ-6438
Rel. protein levels to α-tubulin (MDA-MB-436)
pT980-PERK
pT899-GCN2
M
DMSO
UNC1999 (1 μM)
EPZ-6438 (1 μM)
pT446-PKR
PKR
pT980-PERK
PERK
pT899-GCN2
GCN2
β-actin
68kDa
125kDa
187kDa
42kDa
Hs 578T
N
DMSO
UNC1999
EPZ-6438
Rel. ptn. levels to β-actin (Hs 578T)
pT446-PKR
pT980-PERK
pT899-GCN2
O
DMSO
UNC1999 (1 μM)
EPZ-6438 (1 μM)
Brightfield
TPE-MI
Hs 578T
P
DMSO
UNC1999
EPZ-6438
Relative TPE-MI (Hs 578T)
Q
DMSO UNC1999(1 μM)
siCtl-1
siCtl-2
siGCN2-1
siGCN2-2
GCN2
α-tubulin
187kDa
50kDa
Hs 578T
siPERK-1
siPERK-2
PERK
125kDa
siPKR-1
siPKR-2
PKR
68kDa
siEIF2A-1
siEIF2A-2
eIF2α
36kDa
R
DMSO
UNC1999 (1 μM)
Rel. viability vs siCtl-2 (Hs 578T)
siControl-2
siGCN2-1
siGCN2-2
siPERK-1
siPERK-2
siPKR-1
siPKR-2
siEIF2A-1
siEIF2A-2
S
DMSO
UNC1999 (1 μM)
siControl
siATF4-1
siATF4-2
ATF4
Lamin B1
H3K27me3
H3
49kDa
66kDa
17kDa
GCRC1915 PDC
T
DMSO
UNC1999 (1 μM)
Rel. viability vs siCtl (GCRC1915 PDC)
siControl
siATF4-1
siATF4-2
U
siCtl-1
siCtl-2
siATF4-1
siATF4-2
Relative cl-PAPR levels to Lamin B1
UNC1999 (1 μM)
MDA-MB-436
Hs 578T

Supplementary Figure 2. A. Quantification of the relative pT446-PKR levels from Fig. 2B (rel. to β-actin; N=3). **B.** Immunoblot showing the levels of pT980-PERK, PERK, pT446-PKR, PKR, pS51-eIF2α, eIF2α, ATF4 and β-actin in GCRC1939-PDX exposed to UNC1999 (300 mg/kg; 21 days) or Control (N=3). **C.** Quantification of the relative protein levels from Fig. S2B (rel. to β-actin; N=3). **D.** Quantification of the relative pT446-PKR levels from Fig. 2C (rel. to β-actin; N=3). **E.** IHC staining of ATF4 on GCRC1939-PDX exposed to UNC1999 (300 mg/kg, 21 weeks) or control (N=3). **F.** Quantification of the relative protein levels from Fig. 2D (rel. to β-actin; N=3). **G.** Quantification of the relative protein levels from Fig. 2F (rel. to Lamin B1; N=3). **H.** Immunoblot showing pS51-eIF2α, eIF2α, ATF4 and Lamin B1 levels in Hs 578T cells exposed to UNC1999 or EPZ-6438 (1μM; 48 h) or DMSO (0.2%; N=3). **I.** Quantification of the relative protein levels from Fig. S2H (rel. to Lamin B1; N=3). **J.** Quantification of the relative ATF4 levels from Fig. 2G (rel. to Lamin B1; N=3). **K.** Quantification of the relative protein levels from Fig. 2I (rel. to β-actin; N=3). **L.** Quantification of the relative protein levels from Fig. 2J (rel. to α-tubulin; N=3). **M.** Immunoblot showing the levels of the indicated ISR-related kinases, their phosphorylated form and β-actin in Hs 578T cells exposed to UNC1999 or EPZ-6438 (1μM; 48 h) or DMSO (0.2%; N=3). **N.** Quantification of the relative protein levels from Fig. S2M (rel. to β-actin; N=3). **O.** Detection of unfolded protein load in Hs 578T cells exposed to UNC1999 or EPZ-6438 (1μM; 48 h) or DMSO (0.2%; N=3), using the tetraphenyl ethene maleimide (TPE-MI) probe (IF) detecting misfolded protein loads. Cell density is shown in brightfield. Scale bar, 100μm. **P.** Quantification of misfolded protein load from E showing TPE-MI intensity normalized to naïve media and relative to DMSO (0.2%). **Q.** Immunoblot showing the levels of the indicated proteins (GCN2, PKR, PERK, eIF2α , and α-tubulin) in Hs 578T cells exposed to UNC1999 (1μM; 48 h) or DMSO (0.2%; N=3) and depleted or not for the indicated gene/protein using two siRNAs/gene. **R.** Relative viability (crystal violet) of Hs 578T cells depleted of either GCN2, PKR, PERK, or eIF2α using siRNAs (72 h) or siControl and exposed to EZH2 inhibitor UNC1999 (1μM; 96 h) or DMSO (0.2%; N=3). **S.** Immunoblot showing the levels of the ATF4, Lamin B1, H3K27me3 and total H3 proteins in GCRC1915 PDC exposed to UNC1999 (1μM; 48 h) or DMSO (0.2%; N=3) and depleted of ATF4 using specific siRNAs (72 h). **T.** Relative viability (crystal violet) of GCRC1915-PDC depleted of ATF4 using 2 siRNAs (20nM) and exposed to UNC1999 (1μM; 96 h; N=3). **U.** Quantification of the relative protein levels from Fig. 2O (rel. to Lamin B1;

N=3). Data shown are the mean ± SD from 3 biological replicates. Statistical analysis was performed by two-tailed Student's t test (A, C, F and K), one-way (D, G, I, J, L, N, P and U) and two-way ANOVA (R and T). ns, not significant, *$p < 0.05$, **$p < 0.01$, ***$p < 0.001$, ****$p < 0.0001$. R: replicate #.

FIGURE S3

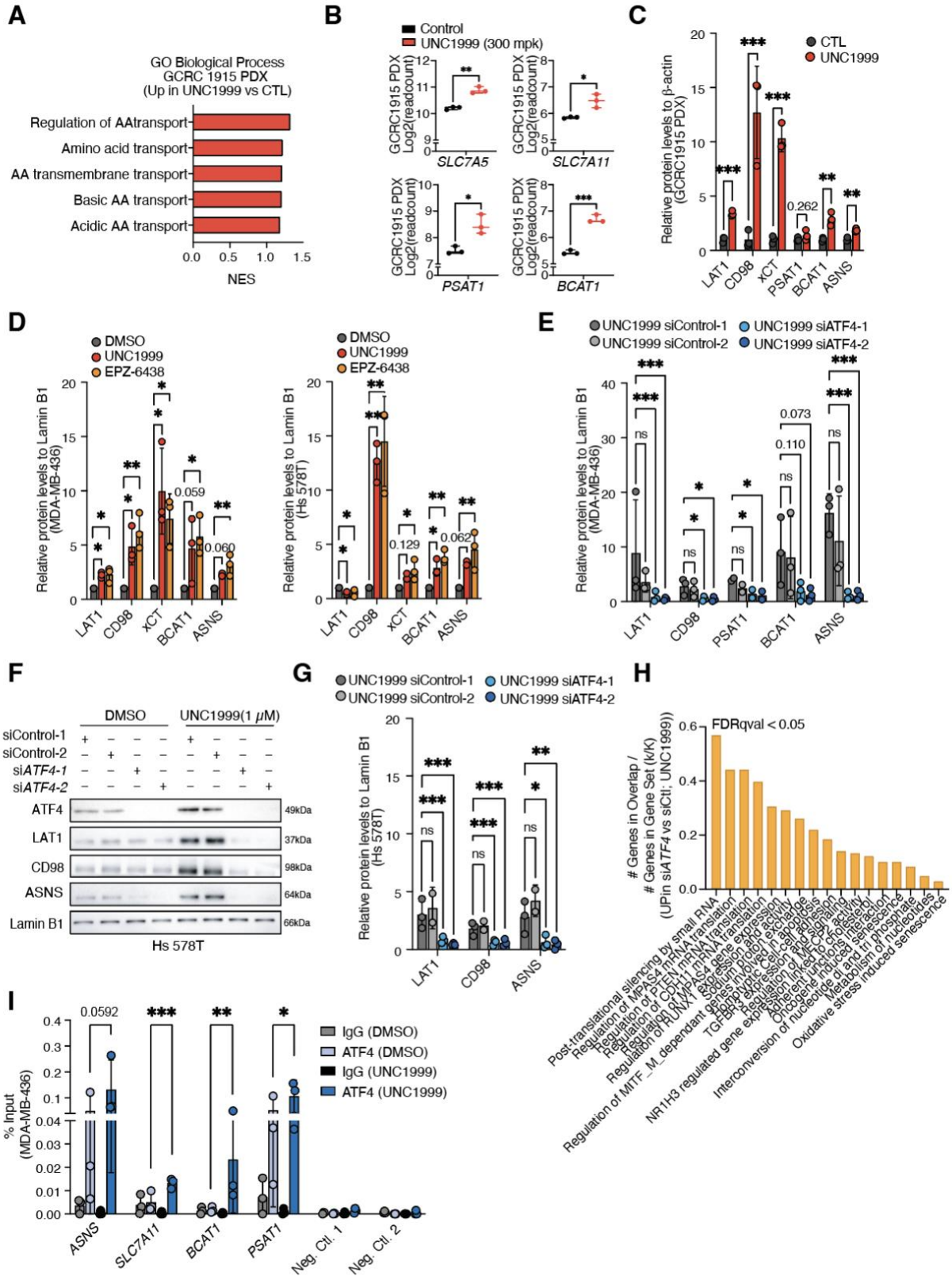

A
GO Biological Process
GCRC 1915 PDX
(Up in UNC1999 vs CTL)
Regulation of AAtransport
Amino acid transport
AA transmembrane transport
Basic AA transport
Acidic AA transport
NES
B
Control
UNC1999 (300 mpk)
GCRC1915 PDX Log2(readcount)
SLC7A5
SLC7A11
PSAT1
BCAT1
C
CTL
UNC1999
Relative protein levels to β-actin (GCRC1915 PDX)
LAT1
CD98
xCT
PSAT1
BCAT1
ASNS
D
DMSO
UNC1999
EPZ-6438
Relative protein levels to Lamin B1 (MDA-MB-436)
Relative protein levels to Lamin B1 (Hs 578T)
E
UNC1999 siControl-1
UNC1999 siControl-2
UNC1999 siATF4-1
UNC1999 siATF4-2
Relative protein levels to Lamin B1 (MDA-MB-436)
F
DMSO
UNC1999(1 μM)
siControl-1
siControl-2
siATF4-1
siATF4-2
ATF4
LAT1
CD98
ASNS
Lamin B1
Hs 578T
G
UNC1999 siControl-1
UNC1999 siControl-2
UNC1999 siATF4-1
UNC1999 siATF4-2
Relative protein levels to Lamin B1 (Hs 578T)
H
FDRqval < 0.05
Genes in Overlap / # Genes in Gene Set (k/K) (UPin siATF4 vs siCtl; UNC1999))
Post-translational silencing by small RNA
Regulation of MPAS4 mRNA translation
Regulation of PTEN mRNA translation
Regulation of CDH1 mRNA translation
Regulation of MPAS4 gene expression
Regulation of MIT_M_dependant genes involved in apoptosis
Regulation of RUNX1 expression and activity
Sodium proton exchange
Eumorphic Cell-cell adhesion
TGFBR3 expression and signaling
Regulation of MECP2 activity
Regulation linked to cholesterol
Adherent junctions interaction
Oncogene induced senescence
Interconversion of nucleotide di and tri phosphate
Metabolism of nucleotides
Oxidative stress induced senescence
I
% Input (MDA-MB-436)
IgG (DMSO)
ATF4 (DMSO)
IgG (UNC1999)
ATF4 (UNC1999)
ASNS
SLC7A11
BCAT1
PSAT1
Neg. Ctl. 1
Neg. Ctl. 2

Supplementary Figure 3. A. GSEA bar graph displaying significantly enriched metabolism-related gene ontology biological process (GOBP) pathways ($p<0.05$), from genes significantly up-regulated in UNC1999-treated GCRC1915-PDX (300 mg/kg; 21 days) relative to control (N=3). **B.** Gene expression levels of *SLC5A7*, *SLC7A11*, *PSAT1* and *BCAT1* in GCRC1915 PDX exposed to UNC1999 (300 mg/kg; 21 days) relative to control (N=3). **C.** Quantification of the relative protein levels from Fig. 3C (rel. to β-actin; N=3). **D.** Quantification of the relative protein levels from Fig. 3D (rel. to Lamin B1; N=3). **E.** Quantification of the relative protein levels from Fig. 3E (rel. to Lamin B1; N=3). **F.** Immunoblot showing the levels of ATF4, LAT1, CD98, ASNS and Lamin B1 in Hs 578T cells exposed to DMSO (0.2%) or UNC1999 (1μM; 72 h) (N=3) and depleted for ATF4 using 2 siRNAs (72 h). **G.** Quantification of the relative protein levels from Fig. S3F (rel. to Lamin B1; N=3). **H.** Bar graph representing down-regulated pathways (Reactome gene set) following ATF4 depletion in MDA-MB-436 cells exposed to UNC1999 (1μM; 48 h) relative to DMSO (0.2%; N=3). **I.** ATF4 Chromatin immunoprecipitation followed by qPCR amplification at specific ATF4 target gene promoters (*ASNS*, *SLC7A11*, *BCAT1,* and *PSAT1*) and two negative control regions in MDA-MB-436 exposed to UNC1999 (1μM; 48 h) or DMSO (0.2%; N=3) (data shown as %input). Data analysis is presented as the mean ± SD from three biological replicates. Statistical analysis was performed by two-tailed Student's t test (B and C) and one-way ANOVA (D, F, G and I). ns, not significant, $*p < 0.05$ $**p < 0.01$, $***p < 0.001$. R: replicate #.

FIGURE S4

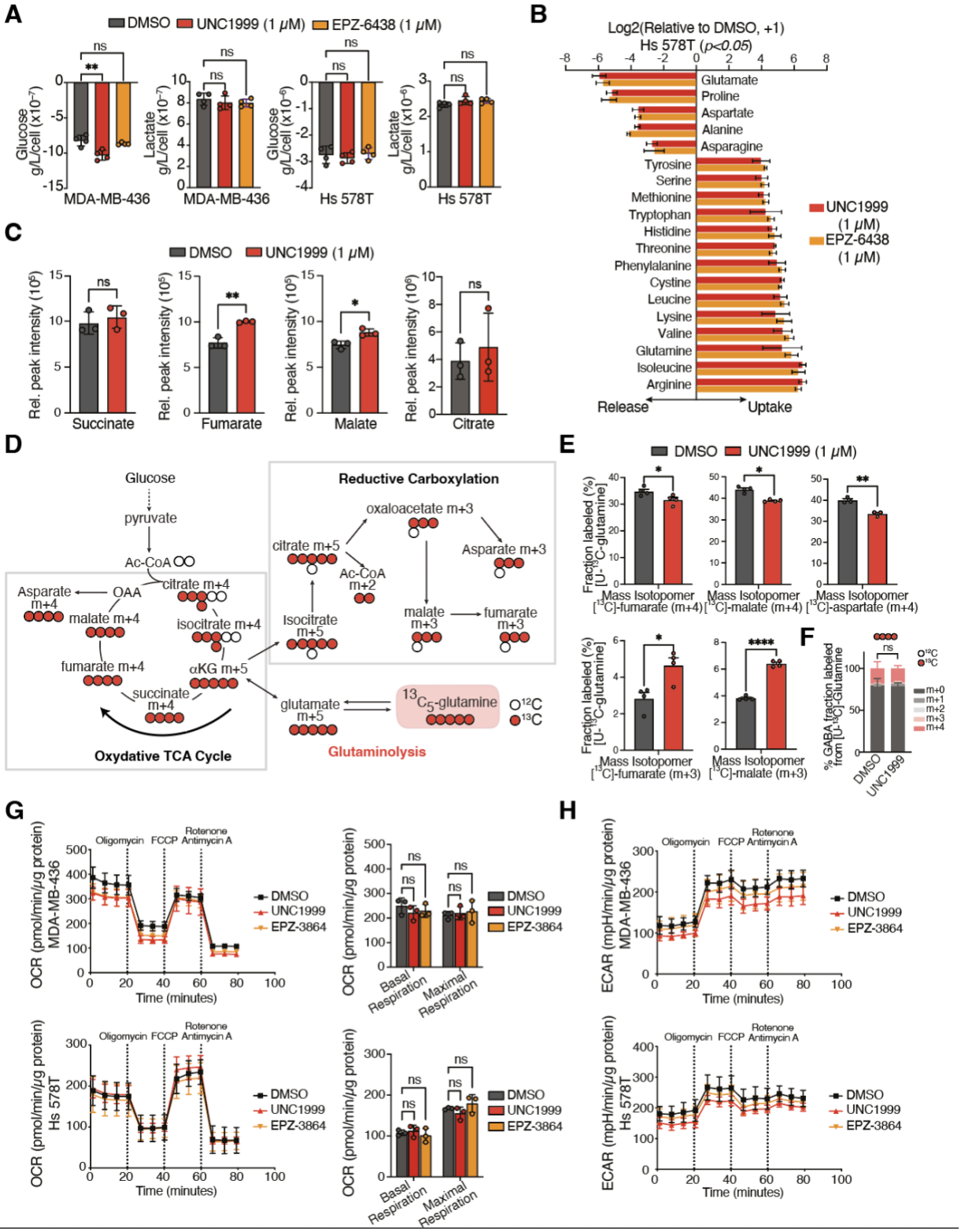
A
DMSO
UNC1999 (1 μM)
EPZ-6438 (1 μM)
Glucose g/L/cell (x10⁻⁷)
Lactate g/L/cell (x10⁻⁷)
Glucose g/L/cell (x10⁻⁶)
Lactate g/L/cell (x10⁻⁶)
MDA-MB-436
MDA-MB-436
Hs 578T
Hs 578T
B
Log2(Relative to DMSO, +1)
Hs 578T (p<0.05)
Glutamate
Proline
Aspartate
Alanine
Asparagine
Tyrosine
Serine
Methionine
Tryptophan
Histidine
Threonine
Phenylalanine
Cystine
Leucine
Lysine
Valine
Glutamine
Isoleucine
Arginine
Release
Uptake
UNC1999 (1 μM)
EPZ-6438 (1 μM)
C
DMSO
UNC1999 (1 μM)
Rel. peak intensity (10⁵)
Rel. peak intensity (10⁶)
Succinate
Fumarate
Malate
Citrate
D
Glucose
pyruvate
Ac-CoA
citrate m+4
OAA
Asparate m+4
malate m+4
isocitrate m+4
fumarate m+4
αKG m+5
succinate m+4
Oxydative TCA Cycle
Reductive Carboxylation
oxaloacetate m+3
citrate m+5
Ac-CoA m+2
Asparate m+3
Isocitrate m+5
malate m+3
fumarate m+3
glutamate m+5
13C5-glutamine
12C
13C
Glutaminolysis
E
DMSO
UNC1999 (1 μM)
Fraction labeled (%) [U-13C-glutamine]
Mass Isotopomer [13C]-fumarate (m+4)
Mass Isotopomer [13C]-malate (m+4)
Mass Isotopomer [13C]-aspartate (m+4)
Mass Isotopomer [13C]-fumarate (m+3)
Mass Isotopomer [13C]-malate (m+3)
F
% GABA fraction labeled from [U-13C]-Glutamine
12C
13C
m+0
m+1
m+2
m+3
m+4
DMSO
UNC1999
G
OCR (pmol/min/μg protein) MDA-MB-436
OCR (pmol/min/μg protein) Hs 578T
Oligomycin
FCCP
Rotenone Antimycin A
Time (minutes)
DMSO
UNC1999
EPZ-3864
Basal Respiration
Maximal Respiration
H
ECAR (mpH/min/μg protein) MDA-MB-436
ECAR (mpH/min/μg protein) Hs 578T
Oligomycin
FCCP
Rotenone Antimycin A
Time (minutes)
DMSO
UNC1999
EPZ-3864

Supplementary Figure 4. A. Relative quantification of glucose and lactate (BioProfile 400, Nova Biomedical) in conditioned media exposed to MDA-MB-436 or Hs 578T cells exposed to UNC1999 or EPZ-6438 (1μM; 72 h) or DMSO (0.2%; N=4; data shown relative to naïve media). **B.** Relative metabolite quantification in conditioned media using QQQ-LC-MS (Intrada-amino-acids) in Hs 578T cells exposed to UNC1999 and EPZ-6438 (1μM; 72 h) or DMSO (0.2%; N=4; $p<0.05$). Metabolite levels for each experimental condition are normalized to those in the naive medium. **C.** Quantification of specific intracellular metabolites in Hs 578T cells by QTOF-LC-MS (Ion-pairing) exposed to UNC1999 (1μM; 72 h) or DMSO (0.2%; N=3). **D.** Schematic representation of the ^{13}C-labeling of glutaminolysis, oxidative TCA cycle, and reductive carboxylation intermediate from $^{13}C_5$-glutamine. **E.** Percentage fraction of ^{13}Carbon-labelled oxidative TCA cycle intermediates (top, fumarate m+4, malate m+4, and aspartate m+4), reductive carboxylation intermediates (bottom, malate m+3, fumarate m+3) in DMSO- and UNC1999-treated (1μM, 96 h) Hs 578T quantified by QTOF-LC-MS (ion pairing) after 2 h exposure to labelled $^{13}C_5$-glutamine (N=4). **F.** Stack bar showing the fraction of ^{13}C-labeled GABA isotopomers in Hs 578T cells exposed to UNC1999 (1μM, 96 h) or DMSO (0.2%; N=4). **G.** Left: Time-dependent Oxygen Consumption Rate (OCR) in MDA-MB-436 (top) and Hs 578T (bottom) cells exposed to UNC1999, EPZ-6438 (1μM; 72 h) or DMSO (0.2%; N=3) upon sequential addition of Oligomycin (1μM), Carbonyl cyanide-p-trifluoromethoxyphenylhydrazone (FCCP; 0.5μM) and Rotenone/AntimycinA (0.5μM). Right: Effect of treatment on OCR basal and maximal respiration is plotted. **H.** Time-dependent Extracellular Acidification Rate (ECAR) in MDA-MB-436 (top) and Hs 578T (bottom) cells exposed to UNC1999, EPZ-6438 (1μM; 72 h) or DMSO (0.2%; N=3) upon sequential addition of Oligomycin (1μM), FCCP (0.5μM) and Rotenone/AntimycinA (0.5μM). Data are the mean ± SD from 3 to 4 biological replicates. Statistical analysis was performed by two-tailed Student's t test (C, E and F) and one-way ANOVA (A, B and G). ns, not significant, *$p < 0.05$, **$p < 0.01$, ***$p < 0.001$, ****$p < 0.0001$.

FIGURE S5

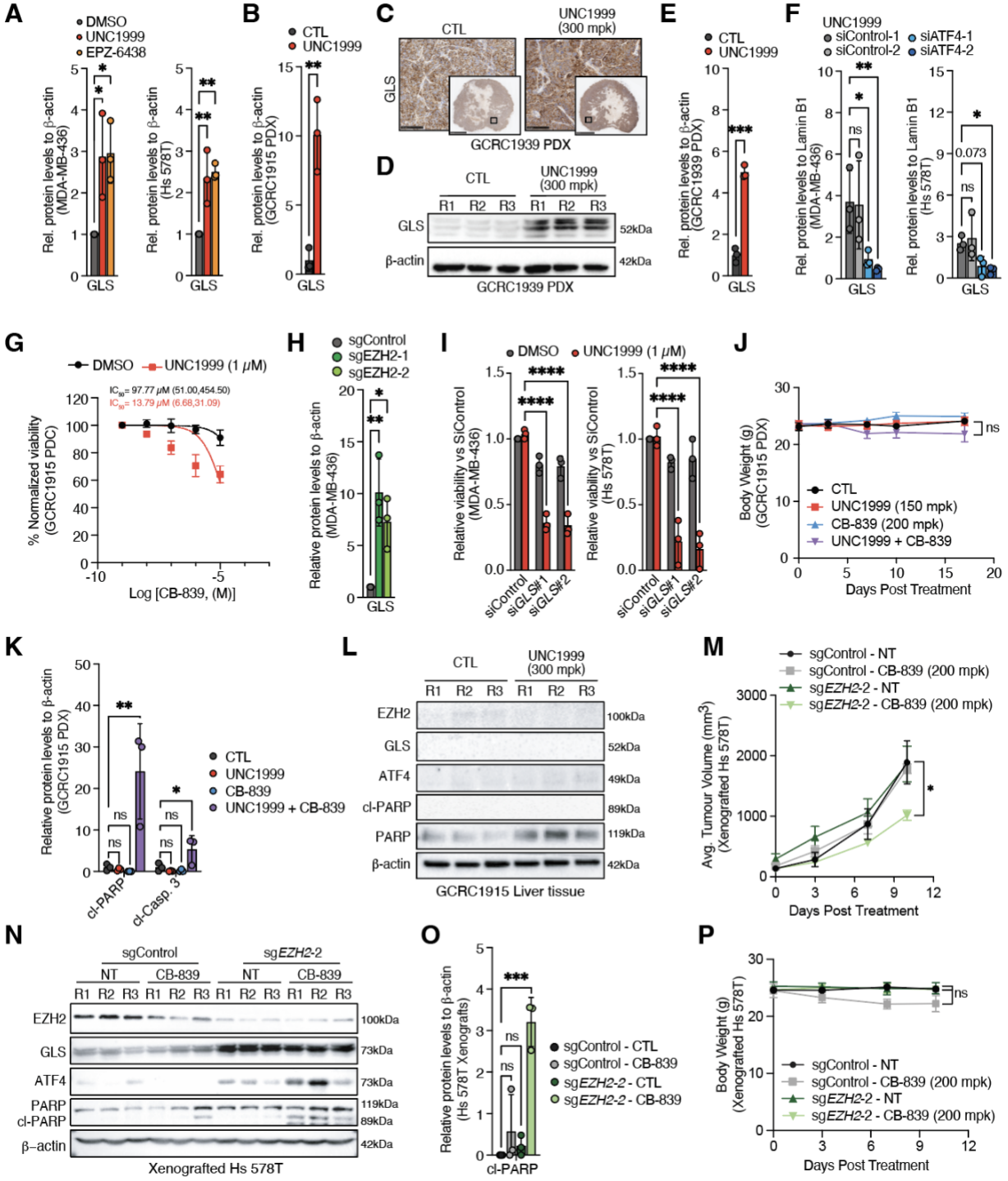
A
DMSO
UNC1999
EPZ-6438
Rel. protein levels to β-actin (MDA-MB-436)
Rel. protein levels to β-actin (Hs 578T)
GLS
B
CTL
UNC1999
Rel. protein levels to β-actin (GCRC1915 PDX)
C
CTL
UNC1999 (300 mpk)
GLS
GCRC1939 PDX
D
CTL
UNC1999 (300 mpk)
R1 R2 R3 R1 R2 R3
GLS
β-actin
52kDa
42kDa
GCRC1939 PDX
E
CTL
UNC1999
Rel. protein levels to β-actin (GCRC1939 PDX)
F
UNC1999
siControl-1
siControl-2
siATF4-1
siATF4-2
Rel. protein levels to Lamin B1 (MDA-MB-436)
Rel. protein levels to Lamin B1 (Hs 578T)
0.073
ns
G
DMSO
UNC1999 (1 μM)
IC50= 97.77 μM (51.00,454.50)
IC50= 13.79 μM (6.68,31.09)
% Normalized viability (GCRC1915 PDC)
Log [CB-839, (M)]
H
sgControl
sgEZH2-1
sgEZH2-2
Relative protein levels to β-actin (MDA-MB-436)
I
DMSO
UNC1999 (1 μM)
Relative viability vs SiControl (MDA-MB-436)
Relative viability vs SiControl (Hs 578T)
siControl
siGLS#1
siGLS#2
J
Body Weight (g) (GCRC1915 PDX)
CTL
UNC1999 (150 mpk)
CB-839 (200 mpk)
UNC1999 + CB-839
Days Post Treatment
K
Relative protein levels to β-actin (GCRC1915 PDX)
CTL
UNC1999
CB-839
UNC1999 + CB-839
cl-PARP
cl-Casp. 3
L
CTL
UNC1999 (300 mpk)
R1 R2 R3 R1 R2 R3
EZH2
GLS
ATF4
cl-PARP
PARP
β-actin
100kDa
52kDa
49kDa
89kDa
119kDa
42kDa
GCRC1915 Liver tissue
M
sgControl - NT
sgControl - CB-839 (200 mpk)
sgEZH2-2 - NT
sgEZH2-2 - CB-839 (200 mpk)
Avg. Tumour Volume (mm3) (Xenografted Hs 578T)
Days Post Treatment
N
sgControl
sgEZH2-2
NT
CB-839
R1 R2 R3 R1 R2 R3 R1 R2 R3 R1 R2 R3
EZH2
GLS
ATF4
PARP
cl-PARP
β-actin
100kDa
73kDa
73kDa
119kDa
89kDa
42kDa
Xenografted Hs 578T
O
Relative protein levels to β-actin (Hs 578T Xenografts)
sgControl - CTL
sgControl - CB-839
sgEZH2-2 - CTL
sgEZH2-2 - CB-839
cl-PARP
P
Body Weight (g) (Xenografted Hs 578T)
sgControl - NT
sgControl - CB-839 (200 mpk)
sgEZH2-2 - NT
sgEZH2-2 - CB-839 (200 mpk)
Days Post Treatment

Supplementary Figure 5. A. Quantification of the relative GLS levels from Fig. 5B (rel. to β-actin; N=3). **B.** Quantification of the relative GLS levels from Fig. 5D (rel. to β-actin; N=3). **C.** Immunohistochemistry (IHC) staining for GLS in GCRC1939 PDX exposed to UNC1999 (300 μM, 21 days) or control (N=3). Magnification, 20X, and scale bars, 100μm. **D.** Immunoblot showing GLS and β-actin levels in GCRC1939 PDX treated with control or UNC1999 (300 mg/kg; 21 days). **E.** Quantification of the relative GLS levels from Fig. S5D (rel. to β-actin; N=3). **F.** Quantification of the relative GLS levels from Fig. 5E (rel. to Lamin B1; N=3). **G.** Dose-response curves representing the relative normalized viability of GCRC1915 PDC cells exposed to DMSO (0.2%) or UNC1999 (1μM; 120h) (N=3) and co-treated with increasing doses of CB-839. IC50 (95% Confidence Interval) was calculated and indicated at the top of the graph. **H.** Quantification of the relative GLS levels from Fig. 5G (rel. to β-actin; N=3). **I.** Relative viability (crystal violet) of MDA-MB-436 and Hs 578T cells depleted of GLS using siRNAs (vs siControl) and exposed to UNC1999 (1μM; 96 h) or DMSO (0.2%; N=3). **J.** Body weight measurements of mice implanted with GCRC1915-PDX and treated as indicated (control, CB-839 (200 mg/kg; 21 days), UNC1999 (150 mg/kg; 21 days), or combination) over 10 days. **K.** Quantification of the relative protein levels from Fig. 5I (rel. to β-actin; N=3). **L.** Immunoblot showing the levels of the EZH2, GLS, ATF4, cl-PARP, and PARP of healthy liver from GCRC1939 PDX exposed to UNC1999 (300 mg/kg; 21 days) or control (N=3). **M.** Average tumor volume over time of sgControl and sg*EZH2* Hs 578T xenografted in female NSG mice exposed to CB-839 (200 mg/kg; 10 days) or control (N=3 per group). **N.** Immunoblot showing the levels of the EZH2, GLS, ATF4, cl-PARP, PARP, and β-actin in xenografted NSG mice either with sgControl or sg*EZH2* Hs 578T cells exposed to CB-839 (200 mg/kg; 10 days) or control (N=3). **O.** Quantification of the relative cl-PARP levels from Fig. S5N (rel. to β-actin; N=3). **P.** Body weight measurements of NGS mice xenografted with Hs 578T sgControl or sg*EZH2* and treated as indicated in G-H. The data shown are the mean ± SD from 3 biological replicates; error bars represent SEM for tumor volume (M). Statistical analysis was performed using one-way (A, F, H, K and O) and two-way ANOVA (I, J, M and P) and two-tailed Student's t test (B and E). ns, not significant, *$p < 0.05$, **$p < 0.01$, ***$p < 0.001$, ****$p < 0.001$. R: replicate #.